PCCP

In- and Ga-Oxo Clusters/Hydrides in Zeolites: Speciation and Catalysis for Light-Alkane Activations/Transformations

Journal:	*Physical Chemistry Chemical Physics*
Manuscript ID	CP-PER-01-2023-000478.R1
Article Type:	Perspective
Date Submitted by the Author:	05-Mar-2023

Complete List of Authors:	Huang, Mengwen; Hokkaido University Yasumura, Shunsaku; Hokkaido University, Institute for Catalysis Toyao, Takashi; Hokkaido university, Institute for Catalysis Shimizu, Ken-ichi; Hokkaido University, Catalysis Research Center Maeno, Zen; Kogakuin University, School of Advanced Engineering

In- and Ga-Oxo Clusters/Hydrides in Zeolites: Speciation and Catalysis for Light-Alkane Activations/Transformations

Huang Mengwen[a],† Shinsaku Yasumura[a],† Takashi Toyao[a], Ken-ichi Shimizu[a], Zen Maeno[b,*]

† H.M and S.Y equally contribute this study.

[a] Institute for Catalysis, Hokkaido University, N-21, W-10, Sapporo 001-0021, Japan

[b] School of Advanced Engineering, Kogakuin University, 2665-1, Nakano-cho, Hachioji, 192-0015, Japan

Corresponding author: zmaeno@cc.kogakuin.ac.jp

Abstract

Metal-exchanged zeolites have great potential to form unique active metal species and develop their catalysis by promoting small molecules such as light alkanes. Ga-exchanged zeolites have attracted attention as promising heterogeneous catalysts for dehydrogenative light-alkane transformations. The speciation of active Ga species in reduced and oxidized Ga-exchanged zeolites and their reaction mechanisms have been discussed in several studies based on experimental and theoretical investigations. In contrast, studies on In-exchanged zeolites have been far less explored, and thus active In-species have rarely been investigated. In this Perspective, we summarized our investigations on In- and Ga-exchanged zeolites for light-alkane transformations. Our research group reported the formation of In–oxo clusters using the O_2 treatment of In-CHA and their potential for the partial oxidation of CH_4 (POM) at room temperature. We also observed the formation of In-hydrides in CHA zeolites during the preparation through reductive solid-state ion-exchange (RSSIE) and revealed their catalysis for non-oxidative C_2H_6 dehydrogenation (EDH). Their detailed structures and reaction mechanisms were discussed in combination with spectroscopic, kinetic, and theoretical studies. Furthermore, comparative studies on the formation of Ga-oxo clusters for POM at room temperature and the controlled formation of Ga-hydrides for selective EDH were conducted. The obtained results and insights were comprehensively discussed, including the relationship between the local structure of the active In/Ga species and reaction selectivity, as well as the influence of different zeolite frameworks on the formation of active species.

1. Introduction

Heterogeneous catalysts are indispensable as key materials in the modern chemical industry to promote and control chemical reactions and reduce the energy consumption in chemical processes, including separation/purification. Among these, zeolites have been widely applied in several chemical processes[1–6] and environmental cleanups[7–12]. One of their features is a crystalline microporous structure consisting of connections between corner-sharing tetrahedral SiO_4 units. Various metal species can be incorporated into their frameworks to afford heteroatomic zeolites. When trivalent metal species such as Al are incorporated, the frameworks possess a negative charge owing to the isomorphic substitution of SiO_4 units with AlO_4 units (Al sites). To compensate for the negative charge, extra-framework cationic species, such as H^+ and NH_4^+, are accommodated at the Al sites in zeolites. These cations can be exchanged with metal cations to synthesize metal-exchanged zeolites, in which the generated cationic species are isolated by zeolite pores. Zeolites have great potential to form unique active metal species and investigate their catalysis to develop effective heterogenous catalysts[13–15].

Group 13 metal-exchanged zeolites have attracted considerable attention for lightalkane transformations, such as Cyclar process[16–18]. Ga-exchanged MFI (Ga-MFI) is one of the most widely studied zeolites. Ono et al. synthesized Ga-MFIs using a liquid-phase ion-exchange method and subsequently used it for the dehydrocyclodimerization (DHCD) of propane to aromatics[19]. To improve the activity of Ga-MFI by loading larger amounts of Ga species, reductive solid-state ion-exchange (RSSIE) under H_2 flow was investigated[20]. Several reduced Ga species, such as Ga^+ cations and Ga-hydrides ($[GaH]^{2+}$ and $[GaH_2]^+$), are considered as catalytically active species for propane (C_3H_8) dehydrogenation (PDH) in the absence of an oxidant[21–23]. Two isolated Ga-hydrides are distinguishable by FTIR measurement because their Ga–H stretching vibration peaks are observed at different wavenumbers[22] Bell and co-workers reported that $[GaH]^{2+}$, as opposed to $[GaH_2]^+$ ions, are active species using a combination of kinetic, spectroscopic, and theoretical studies[24], whereas Lewis–Brønsted acid pairs (Ga^+ and H^+) have been proposed as active sites by the Lercher's group based on characterization and catalytic investigation of a series of Ga-MFIs with different Ga/Al ratios and theoretical investigations[25]. Various Ga-exchanged zeolites, including Ga-MFI, have been applied to the transformation of other light alkanes to aromatic compounds, dehydrogenation of light alkanes, and reactions of CH_4 with light alkenes to produce higher hydrocarbons[26–28]. Studies on the use of oxidized Ga species for alkane activation have also been reported. For example, the formation and catalysis of Ga-oxo clusters during H_2O-accelerated alkane dehydrogenation were discussed by Hensen et al[29,30]. Regardless of whether they are reduced and oxidized, the reaction mechanism of alkane

activation over possible Ga species has been theoretically discussed[31–35]. Several reaction pathways, including alkyl, carbenium, or concerted mechanisms over possible reduced Ga cations (Ga^+, $[GaH]^{2+}$, and/or $[GaH_2]^+$) have been considered in the density functional theory studies for non-oxidative alkane dehydrogenation utilizing cluster models.[32,33,35] The recent study using a hybrid quantum mechanics/molecular mechanics model provided the reasonable activation barrier values similar to the experimentally obtained ones where isolated Ga hydrides were predicted to be more active than Ga^+ cations.[31] A few oxidized Ga cations, such as $[GaO]^+$ and $[Ga_2O_2]^{2+}$, were considered as possible active sites for alkane dehydrogenation in the presence of oxidants.[34]

In contrast to Ga-exchanged zeolites, few studies on catalysis by In-exchanged zeolites have been reported. In-exchanged zeolites can be prepared through RSSIE between In_2O_3 and proton-type zeolites to yield In^+ cations[36]. In the context of catalysis, Hart et al. reported that In-MFI exhibited inferior activity and durability for the DHCD of C_3H_8[37,38]. Baba et al. found that the coupling reaction of CH_4 with ethylene/benzene using In-MFI[39]. Isolated InO^+ ions were considered as active sites in the selective catalytic reduction of NO with CH_4 and O_2[40,41], as well as the H/D exchange reaction[42] and transformation of CH_4[43]. However, the local structure of the active In species in zeolites based on spectroscopic and theoretical studies has not been extensively investigated.

Recently, our research group reported the formation of In–oxo clusters by the O_2 treatment of In-CHA and their potential for the partial oxidation of CH_4 (POM) at room temperature[44]. We also found the formation of In-hydrides in CHA zeolites during RSSIE and their selective catalysis for non-oxidative C_2H_6 dehydrogenation (EDH)[45]. Furthermore, comparative studies on the formation of Ga-oxo clusters for room-temperature POM[46] and the controlled formation of Ga-hydrides for selective EDH[47] were conducted. In this Perspective, our recent work on the speciation of active In and Ga species in zeolites for partial CH_4 oxidation and selective C_2H_6 dehydrogenation based on a combination of experimental and theoretical investigations is briefly introduced[44–49].

2. In–oxo clusters in CHA zeolites for room-temperature POM [44]

The POM over Cu–and Fe–oxo clusters under mild reaction conditions has been extensively studied to mimic the catalytic activity of methane mono-oxygenase[50–53]. The POM to methanol (MeOH) undergoes over O_2-activated Cu-MFIs, where di-nuclear $[Cu(O)Cu]^{2+}$ clusters were identified as the active sites[50,51]. The formation of trinuclear $[Cu_3O_3]^{2+}$ in mordenite has also been reported for CH_4 conversion to MeOH based on spectroscopic and theoretical studies[53]. Regarding Fe–oxo clusters, $[Fe_2(\mu_2\text{-}OH)_2(OH)_2(H_2O)_2]^{2+}$ dimers have been proposed as active sites for direct CH_4 oxidation to MeOH in aqueous mediums[54]. Other

transition metal–oxo clusters have been studied experimentally and/or theoretically for CH_4 oxidation[55–58]. In contrast, metal–oxo clusters of typical metal elements for CH_4 oxidation under mild reaction conditions have rarely been reported.

Based on the potential of In-exchanged zeolites for light-alkane activation, we conducted experimental and theoretical studies on the formation of In–oxo clusters for CH_4 activation. Multinuclear In–oxo clusters were generated by O_2 activation of In-CHA (InOx–CHA), as indicated by X-ray absorption spectroscopy (XAS) and *ab initio* thermodynamic analysis. The ability for CH_4 activation was evaluated by monitoring the reaction of CH_4 over InOx–CHA using *in-situ* Fourier transform infrared (FTIR) measurements, as well as transition state (TS) calculations of C–H bond cleavage over plausible In–oxo models.

In-exchanged zeolites can be prepared using RSSIE[59,60]. The In_2O_3-modiifed CHA zeolite (In_2O_3/CHA) was treated under H_2 flow at 500 °C to produce In-exchanged CHA (In-CHA). Thereafter, In-CHA was activated with O_2 at 500 °C to synthesize InOx–CHA. The color of In_2O_3/CHA, prepared by a simple impregnation method, was pale yellow, indicating the presence of bulk In_2O_3, whereas that of InOx–CHA was white, suggesting the formation of In–oxo species, unlike bulk In_2O_3 (Figure 1). The absence of bulk In_2O_3 after the O_2 activation of In-CHA was supported by the X-ray diffraction (XRD) measurements and scanning transmission electron microscope (STEM) observations (Figure 2). *In-situ* K-edge XAS measurements revealed that the absorption edge position of InOx–CHA was similar to that of In_2O_3. In the FT of extended X-ray absorption fine structure (EXAFS) spectrum, the scattering peak derived from In–(O)–In was considerably low compared to that of In_2O_3 (the coordination number (CN) was determined to be 2.4), suggesting the formation of In–oxo clusters by O_2 activation of In-CHA (Figure 3).

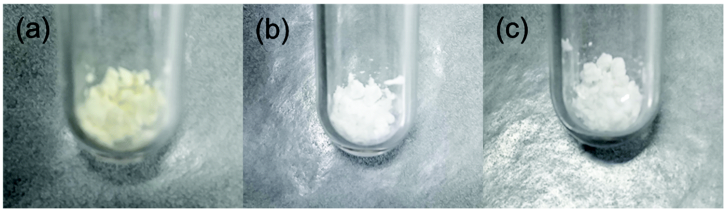

Figure 1. Photographs of (a) In_2O_3/CHA, (b) In-CHA, and (c) InOx–CHA.

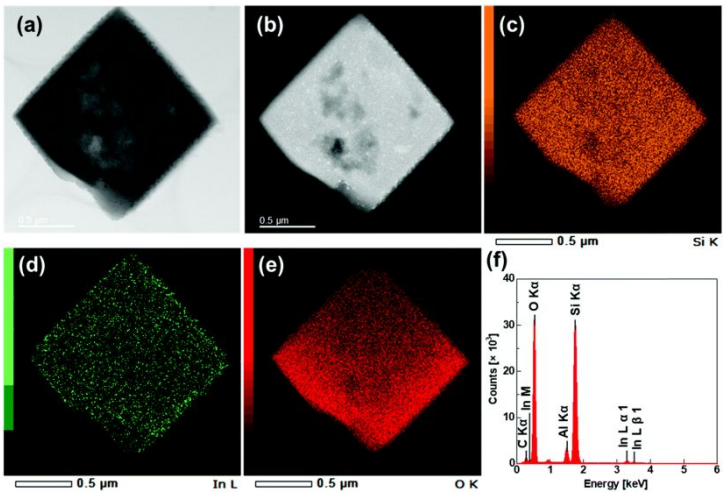

Figure 2. (a) Annular bright-field and (b) high angle annular dark-field STEM images of InOx–CHA. Elemental mapping images of (c) Si, (d) In, (e) O, and (f) EDX spectrum.

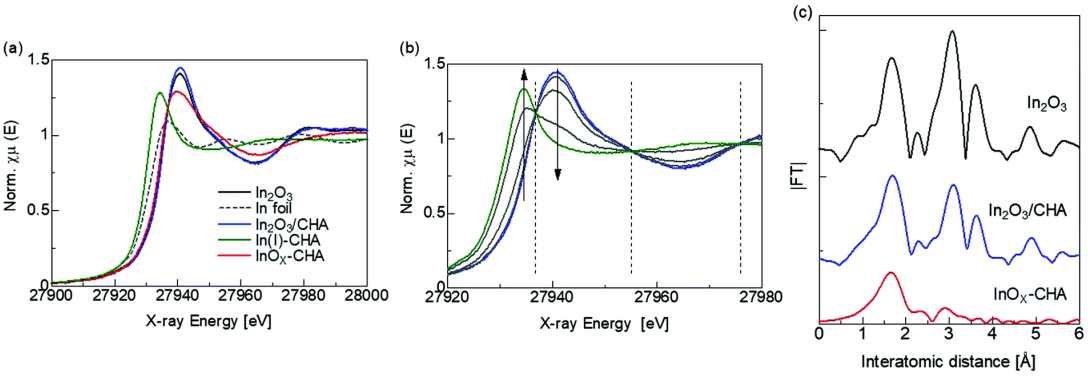

Figure 3. (a) Normalized In K-edge K-ray absorption near edge structure (XANES) spectra of In_2O_3, In-foil, In_2O_3/CHA, In-CHA (after H_2 treatment of In_2O_3/CHA), and InOx–CHA (after O_2 treatment of In_2O_3/CHA). (b) *In-situ* In-K-edge XANES spectra during H_2 treatment of In_2O_3/CHA. Dotted lines indicate isosbestic points. (c) FT of k^3-weighted EXAFS oscillations measured at room temperature for In_2O_3, In_2O_3/CHA, and InOx–CHA.

To predict the possible structure of In–oxo clusters, *ab initio* thermodynamic analysis was performed. This approach is useful for predicting the structures of key multinuclear metal–oxo clusters of transition metal cations in zeolites[61–63]. The formation of monomers, dimers, trimers, and tetramers on three different types of paired Al sites (8MR(3NN), 8MR(4NN), and 6MR(3NN), Figure 4) was considered, whereas the effect of the partial pressure of O_2 and H_2O during the O_2 treatment was included as the chemical potential. It is predicted that the formation of In–oxo clusters, such as $[In_2O_2]^{2+}$ and $[In_4O_4]^{2+}$, is favored over 8MR(4NN), whereas the monomeric In–oxo species, $[In(OH)]^{2+}$, is thermodynamically more stable than In–oxo clusters over 6MR(3NN). In the case of 8MR(3NN), $[In_2O_2]^{2+}$ is the most plausible

structure of In–oxo clusters, although monomeric $[In(OH)]^{2+}$ is slightly more stable than $[In_2O_2]^{2+}$ (Figure 5).

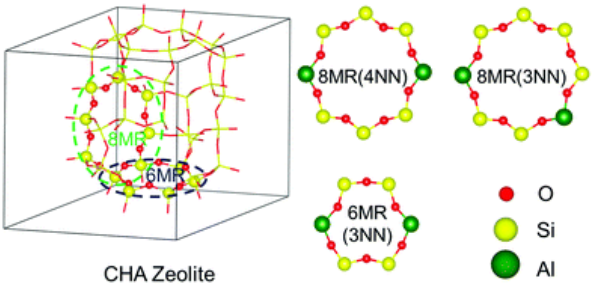

Figure 4. CHA unit cell and Al configuration investigated using periodic DFT calculations. Ovals highlight the locations of 8MR and 6MR.

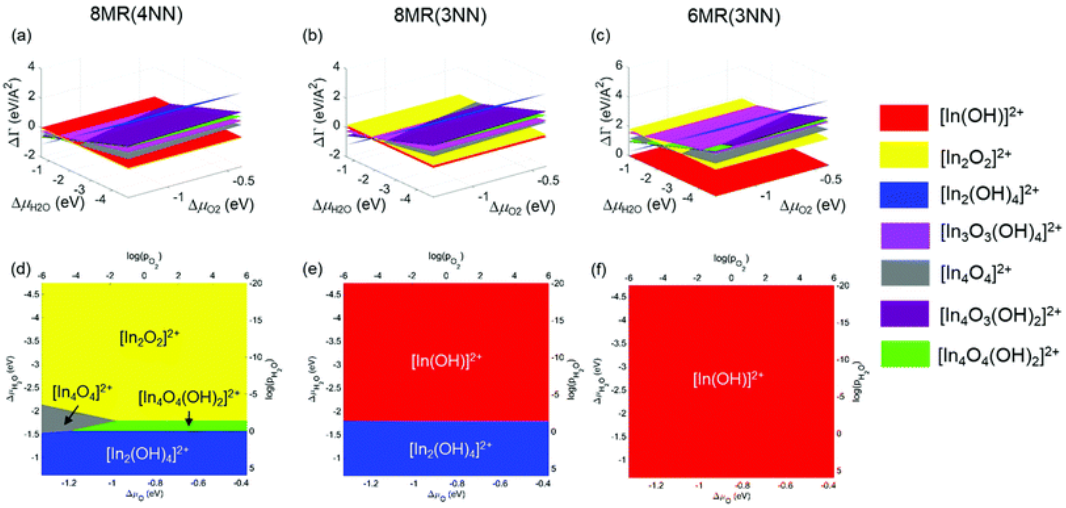

Figure 5. Free energy ($\Delta\Gamma$) for the formation of the In–oxo ions in CHA (top) and phase diagram showing the lowest-energy In–oxo ions (bottom) as a function of O_2 and H_2O chemical potentials ($\Delta\mu_{O2}$ and $\Delta\mu_{H2O}$, respectively) on (a and d) 8MR(4NN), (b and e) 8MR(3NN), and (c and f) 6MR(3NN).

The CH_4 activation ability of In–oxo clusters was explored using *in-situ* FTIR spectroscopy. Under CH_4 flow at room temperature, two absorption bands derived from the C=O stretching and C-H bending of adsorbed formic-acid species were observed between 1600–1800 cm^{-1} and 1300–1500 cm^{-1}, respectively. CO_2 and CO were not detected in the gas phase, indicating the occurrence of POM to adsorbed formic acid species. When bulk In_2O_3 or proton-exchanged CHA zeolites were used instead of InOx–CHA, the IR spectra did not contain peaks derived from oxygen-containing products. The POM at room temperature occurred over the In–oxo clusters (Figure 6).

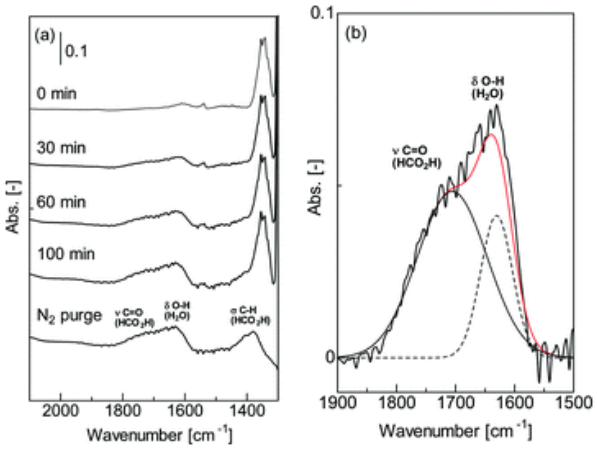

Figure 6. (a) FTIR spectra of InOx–CHA during reaction with CH_4 at room temperature. (b) Curve fitting of the band (1800–1600 cm^{-1}) in the IR spectrum after N_2 purging.

To support the occurrence of CH_4 activation, the C–H cleavage over four possible In–oxo species was studied. The C–H cleavage of CH_4 over $[In_2O_2]^{2+}$ at 8MR(4NN) occurs heterolytically at the In–O bond to form In–CH_3 and O–H bonds. The theoretical activation barrier (E_{a_theo}) of C–H bond cleavage was calculated as approx. 90 kJ/mol, which is reasonable for CH_4 activation under mild conditions. The E_{a_theo} value for monomeric $[In(OH)]^{2+}$ at 6MR(3NN) (approx. 120 kJ/mol) is higher than that for $[In_2O_2]^{2+}$ at 8MR(4NN). The $[In_2O_2]^{2+}$ dimer at different paired Al sites (8MR(3NN)) showed almost the same E_{a_theo} value (approx. 90 kJ/mol), whereas the E_{a_theo} for the $[In_4O_4]^{2+}$ tetramer was higher (approx. 110 kJ/mol) than that for the $[In_2O_2]^{2+}$ dimer model (Figure 7). $[In_2O_2]^{2+}$ dimers are more plausible structures than mononuclear or tetranuclear In–oxo species. Molecular orbital analysis of CH_4 activation over $[In_2O_2]^{2+}$ at 8MR(4NN) indicated that charge transfer from the highest occupied molecular orbital (HOMO) of CH_4 to the lowest unoccupied molecular orbital (LUMO) of $[In_2O_2]^{2+}$ is more likely to occur than that from the HOMO of $[In_2O_2]^{2+}$ to the LUMO of CH_4[64–66]. The ΔE_{a_theo} for radical cleavage is predicted to be considerably high (> 200 kJ/mol), supporting our hypothesis that the C–H bond cleavage of CH_4 occurs in a heterolytic manner.

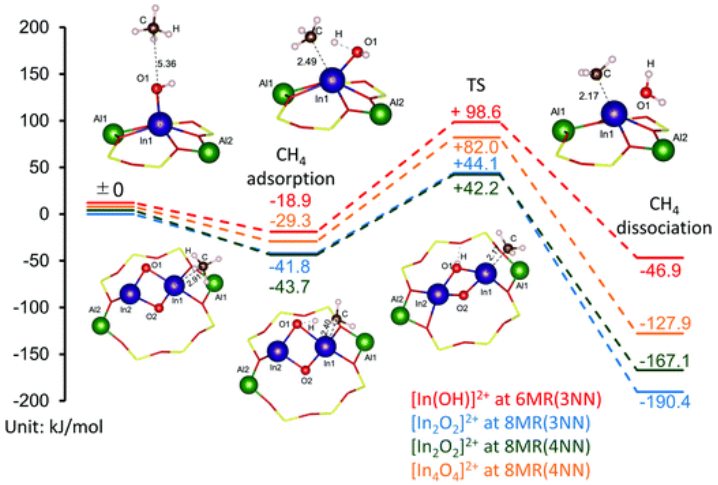

Figure 7. Reaction energy diagrams of intermediates and transition states for the activation of CH_4 by $[In_2O_2]^{2+}$-8MR(4NN) (green), $[In_2O_2]^{2+}$-8MR(3NN) (blue), $[In(OH)]^{2+}$-6MR(3NN) (red), and $[In_4O_4]^{2+}$-8MR(4NN) (orange). Optimized structures of the intermediates and transition states of $[In_2O_2]^{2+}$-8MR(4NN) (bottom) and $[In(OH)]^{2+}$-6MR(3NN) (top) are included in the figure.

3. Ga-oxo cluster in CHA zeolites for room-temperature POM [46]

Although Ga-zeolites have been extensively studied for alkane transformations, as described in Introduction, the formation and catalysis of Ga-oxo species have been less studied than those of reduced Ga species. The formation of Ga-oxo clusters during H_2O-accelerated alkane dehydrogenation over Ga-exchanged zeolites was proposed by Hensen et al.[29,30]. Other studies on Ga-oxo species for alkane activation/transformation have been reported in a limited number of studies[67–69]. However, CH_4 activation at room temperature over Ga-oxo species in zeolites has not been reported. Based on our finding in the study on InOx–CHA, we further investigated the experimental and theoretical study on the formation of Ga-oxo clusters for CH_4 activation as a comparative study with In–oxo clusters.

Ga-exchanged zeolites can also be prepared by RSSIE. The H_2 temperature-programmed reduction (TPR) profile during the RSSIE of the Ga_2O_3-modified CHA zeolites (Ga_2O_3/CHA) showed a reduction peak at approximately 600–700 ˚C (Figure 8). This temperature range is higher than that of InOx–CHA (300–500 ˚C)[44]. *In-situ* Ga K-edge XAS measurements during RSSIE under H_2 flow at 700 °C revealed that the absorption edge shifted toward lower energy values by c.a. 4–5 eV (Figure 9). This shift is interpreted as the formation of reduced Ga species in zeolites, such as isolated Ga^+ cations and Ga-hydrides ($[GaH_2]^+$ and $[GaH]^{2+}$), although the detailed assignment is still controversial[70–73]. After O_2 activation of Ga-exchanged CHA (Ga-CHA) at 500 °C, the absorption edge returned toward higher energy,

and its energy value was similar to that of β-Ga_2O_3. The XANES spectrum of the O_2-activted Ga-CHA (denoted as GaOx-CHA) contained mainly one peak assignable to tetrahedral Ga^{3+} species, whereas two peaks were observed in the XANES spectrum of β-Ga_2O_3[74] indicating that highly dispersed oxidized Ga species existed after O_2 activation. The curve-fitting analysis of FT of EXAFS indicated that the CN of Ga–(O)–Ga was 1.06, which is much lower than that for β-Ga_2O_3 (CN is theoretically above 4), suggesting the presence of Ga-oxo clusters.

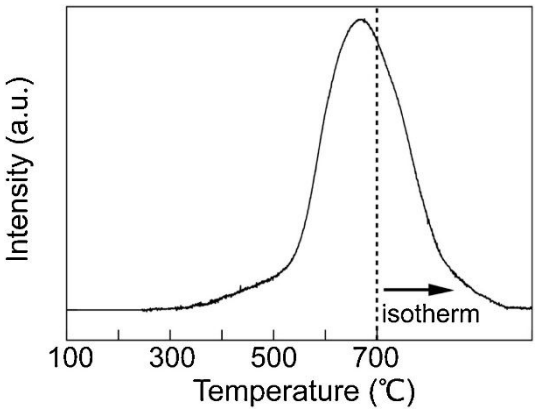

Figure 8. H_2-TPR profile of Ga_2O_3/CHA under H_2 flow. Reprinted with permission from ref 46. Copyright 2020 Elsevier.

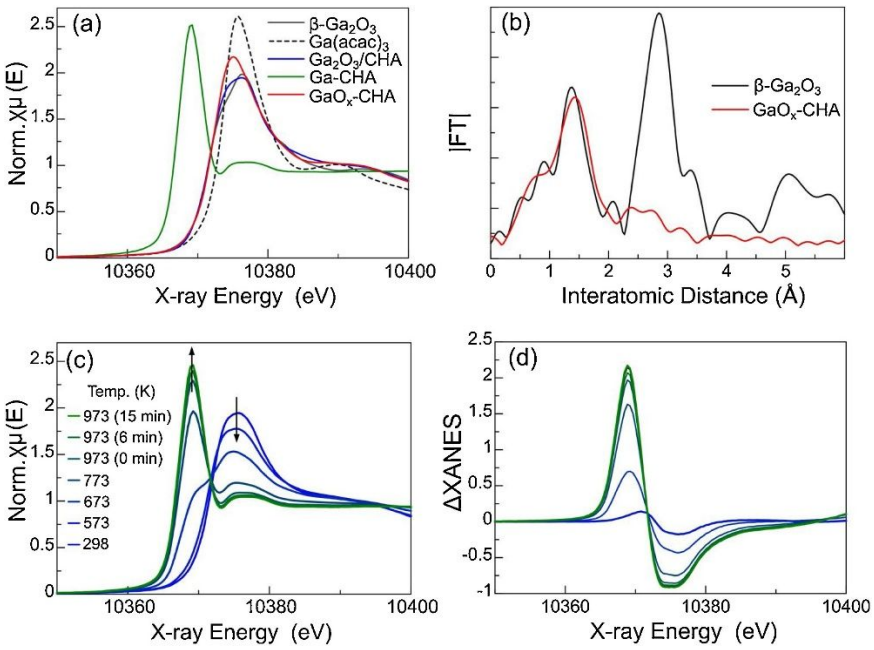

Figure 9. (a) Normalized Ga K-edge XANES spectra of β-Ga_2O_3, $Ga(acac)_3$, Ga_2O_3/CHA, Ga-CHA (after H_2 treatment of Ga_2O_3/CHA at 700 °C), and GaOx-CHA (after O_2 treatment of Ga-CHA at 500 °C). (b) FT of k^3-weighted EXAFS oscillations measured at room temperature for β-Ga_2O_3 and GaOx-CHA. (c) *In-situ* Ga K-edge XANES spectra during H_2

treatment of Ga_2O_3/CHA. (d) Corresponding ΔXANES spectra obtained by subtracting the Ga_2O_3/CHA spectrum at the beginning of H_2 treatment at room temperature. Reprinted with permission from ref 46. Copyright 2020 Elsevier.

The plausible structure of the Ga-oxo species in GaOx-CHA was also discussed by *ab initio* thermodynamics analysis. The same three paired Al sites, 8MR(4NN), 8MR(3NN), and 6MR(3NN), were considered as coordination sites for the Ga-oxo species. Phase diagrams predicting the most stable species (Figure 10) revealed that the lower-temperature region was favorable for the formation of $[Ga_2(OH)_4]^{2+}$ dimers. In the high-temperature region, monomeric $[Ga(OH)]^{2+}$ is the most stable on 6MR(3NN), whereas the $[Ga_2O_2]^{2+}$ dimer is the most stable on 8MR(3NN) and (4NN). The relatively stable species $[Ga_2(O)(OH)_2]^{2+}$ and $[Ga_3(O)_2(OH)_3]^{2+}$ were also predicted.

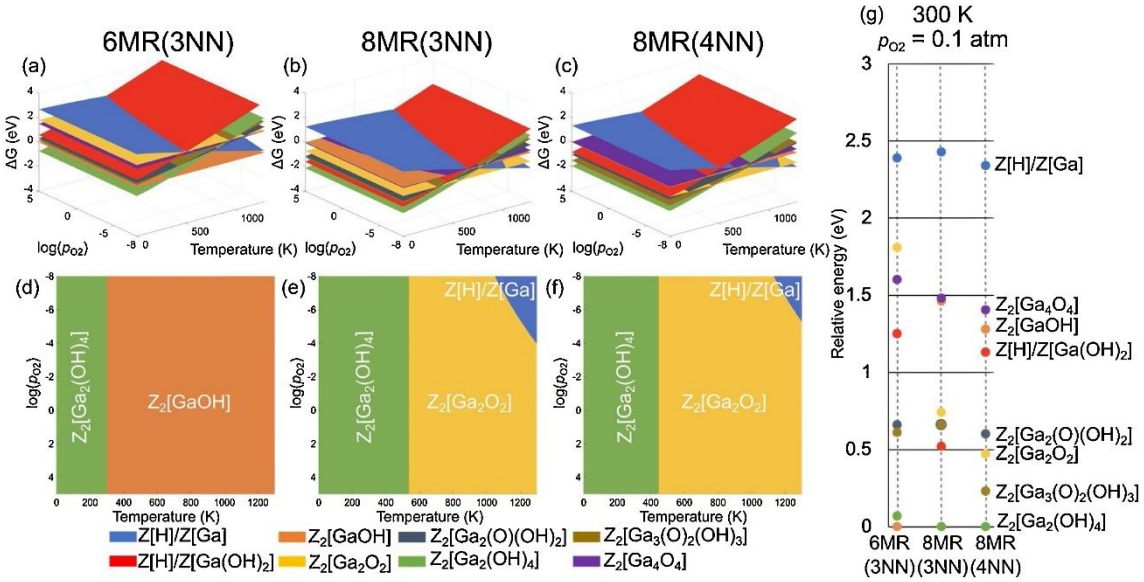

Figure 10. Free energy (ΔG) for the formation of Ga(-oxo) ions on paired Al sites (Z_2) in CHA (top) and the phase diagram showing the lowest-energy species (bottom) as a function of the O_2 partial pressure (log(p_{O2})) and temperature for (a, d) 8MR(4NN), (b, e) 8MR(3NN), and (c, f) 6MR(3NN). (g) Relative energies of Ga(-oxo) ions at each paired Al site, referenced to the lowest-energy Ga-oxo ions, with O_2 partial pressure = 0.1 atm and temperature = 27 °C. Reprinted with permission from ref 46. Copyright 2020 Elsevier.

To examine the ability of CH_4 activation at room temperature, the surface-adsorbed species generated under CH_4 flow at room temperature were monitored by *in-situ* FTIR measurements. In contrast to the case of InOx–CHA in our previous study, a narrow peak appeared at 1490 cm^{-1}, which can be attributed to scissoring of the surface dioxymethylene species (–OCH_2O–, adsorbed formaldehyde species). The deconvolution of the absorption

band at approximately 1400 cm^{-1} revealed that the peak derived from the wagging of surface $–OCH_2O–$ groups also appeared at 1413 cm^{-1}, with the peak derived from the C–H bending of adsorbed HCO_2H (Figure 11). This supports the formation of surface formaldehyde species, which is different from the case of InOx–CHA. In both cases of InOx- and GaO-CHA, it was difficult to extract the adsorbed products using solvents such as D_2O, resulting in difficulty in determining turnover number values.

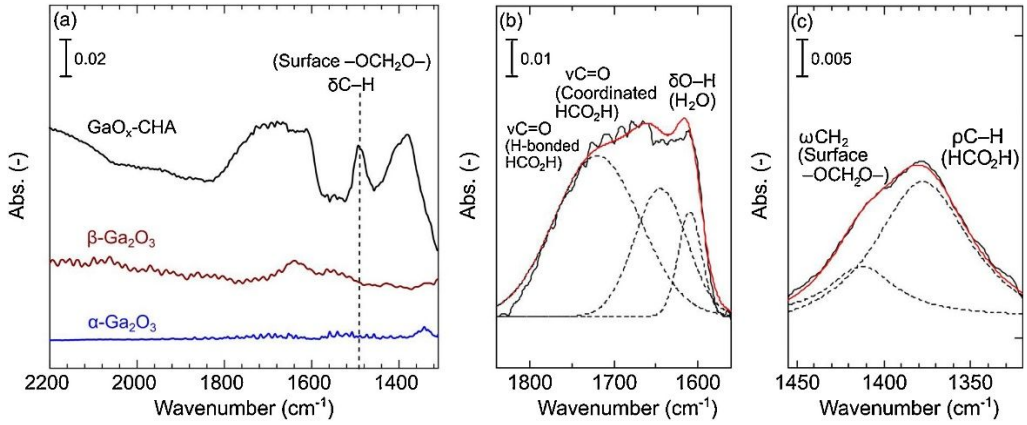

Figure 11. (a) FTIR spectra of the reaction of CH_4 with GaOx-CHA at room temperature. Deconvolution of the bands at approximately (b) 1700 cm^{-1} and (c) 1400 cm^{-1}. Reprinted with permission from ref 46. Copyright 2020 Elsevier.

The C–H bond cleavage of CH_4 over Ga-oxo clusters in CHA zeolites was also studied by DFT calculations to determine a plausible Ga-oxo species that is active for partial CH_4 oxidation. Based on the results of *ab initio* thermodynamics analysis, five model structures with different nuclearities and structures were considered (Figure 12). The calculated adsorption energies were similar regardless of the different structures (approx. 20–30 kJ/mol). In contrast, only $[Ga(O)(OH)_2]^{2+}$ exhibited a relatively low E_{a_theo} less than 100 kJ/mol, which is approximately half of the E_{a_theo} for the monomeric $[Ga(OH)]^{2+}$ model (approx. 180 kJ/mol). The E_{a_theo} for three Ga-oxo cluster models ranged from approximately 130 to 160 kJ/mol (Figure 13). Among the tested Ga-oxo species, $[Ga(O)(OH)_2]^{2+}$ is the most plausible structure. Regarding the reaction mechanism, the C–H bond of CH_4 is likely to undergo heterolytic rather than radical reactions. The different products of room-temperature CH_4 oxidation between InOx- and GaOx-CHA, which was experimentally demonstrated by *in-situ* FTIR spectroscopy, are ascribed to the different activities of In–oxo and Ga-oxo clusters in CHA zeolites, as indicated by DFT calculations.

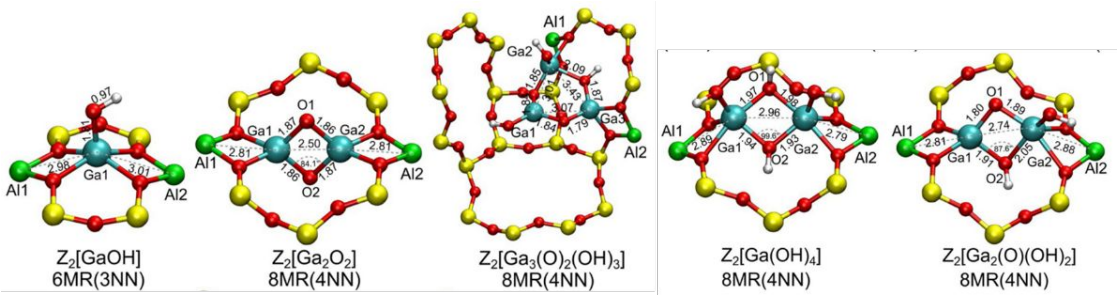

Figure 12. Plausible Ga-oxo species on paired Al sites in CHA zeolite. Reprinted with permission from ref 46. Copyright 2020 Elsevier.

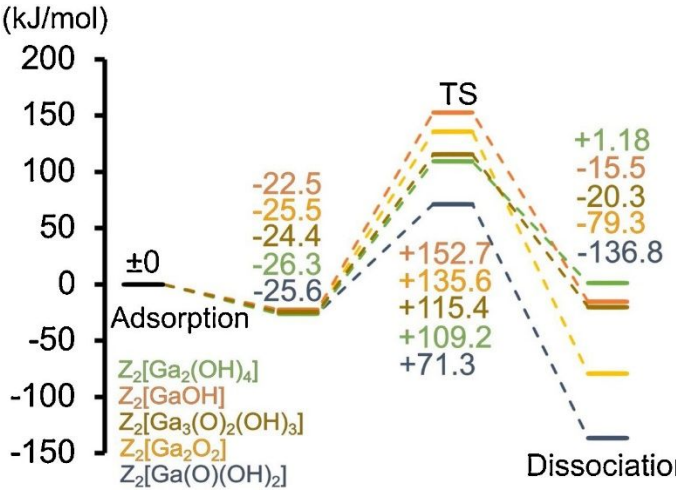

Figure 13. DFT(PBE)-calculated energy diagrams of C–H bond cleavage reactions over the predicted Ga-oxo species. Energies are given in kJ/mol and include the vdW-D3 dispersive correction. Reprinted with permission from ref 46. Copyright 2020 Elsevier.

4. Isolated In-hydrides in CHA zeolite for selective EDH [45]

Surface-isolated hydrides have been studied since the 1970s as key species for hydrogenation, dehydrogenation, and hydrogenolysis reactions of heterogeneous catalysts[75,76]. The reported studies are classified into two main groups: (1) cleavage of H_2 on metals and metal oxides to produce metal-hydrogen (M–H) bonds[77–84] and (2) hydrogenolysis of organometallic species on metal oxides to synthesize well-defined metal hydrides (surface organometallic chemistry (SOMC))[85–89]. Despite the fact that various transition metal hydrides have been synthesized, these hydrides are unstable and thermally decomposed at high reaction temperatures above 200–300 ˚C, resulting in limited catalytic applications. Zeolites are also potential supports for the formation of isolated metal hydrides because well-defined–cation-exchange sites are available in their pores [90,91]. As mentioned above, several research groups have studied the formation and catalysis of isolated Ga-

hydride. The formation and speciation of zeolite-supported Zn[92–94], Ag[95], and Rh hydrides[96] were also revealed by several spectroscopic techniques with the aid of theoretical investigations. Compared to SOMC systems, zeolite-supported isolated metal hydrides have been much less frequently reported. The study of synthesis and catalysis of surface metal hydrides remains a formidable task.

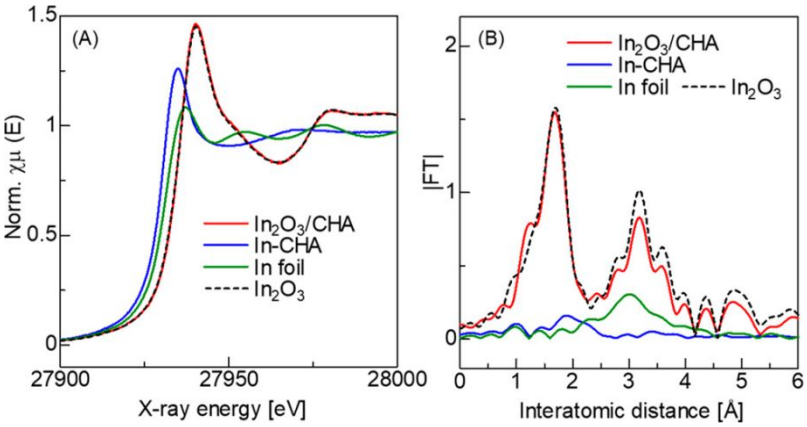

Figure 14. (A) In K-edge XAFS spectra of In-CHA after RSSIE under a H_2 atmosphere at room temperature, the corresponding precursor (In_2O_3/CHA at room temperature), and reference samples (In_2O_3, In foil). (B) Corresponding FT of the EXAFS spectra. Reprinted with permission from ref 45. Copyright 2020 American Chemical Society.

The presence of isolated indium hydrides in CHA zeolites was first determined by *in-situ* In K-edge XANES measurements. Before RSSIE (In_2O_3/CHA), the XANES spectrum and its absorption edge were similar to those of In_2O_3 (Figure 14A). During the RSSIE of In_2O_3/CHA to prepare In-exchanged CHA (In-CHA), the XAFS spectrum of In-CHA showed no scattering peak in the EXAFS region (Figure 14B). A similar disappearance of EXAFS features during RSSIE was observed in *an in-situ* Ga K-edge XAFS study of Ga-exchanged zeolites by Iglesia et al[70]. The absorption edge shifted toward a lower energy value by ca. 4 eV, and its energy value was different from that of the In foil. This edge shift is also similar to the case of *in-situ* Ga K-edge XANES during RSSIE of Ga-modified zeolites as described above[70–73]. Hock et al. discussed that the shift of the absorption edge in the In K-edge XANES spectra of SiO_2-supported In ions during H_2 treatment is interrupted by the formation of In-hydrides, despite the unsuccessful observation of In−H groups by other spectroscopic techniques. Our results were obtained using *in-situ* In K-edge XANES measurements and implied the formation of reduced In species, including In-hydrides.

To investigate the formation of In-hydrides, we performed *in-situ* FTIR measurements, including isotope experiments. The FTIR spectrum of In-CHA after H_2 treatment (denoted as In-CHA(H_2)) showed an absorption band assignable to the In−H stretching vibration at 1720

cm^{-1} (Figure 15). The introduction of ethylene at 200 °C resulted in the disappearance of this band and the appearance of other bands derived from the C−H stretching vibration of adsorbed ethane and/or ethyl fragments, indicating the occurrence of the reaction between In-hydrides and ethylene. When In-CHA was treated with D_2 (denoted In-CHA(D_2)), the band derived from In−H was not observed. In the reaction of In-CHA(D_2) with ethylene, a new band assignable to the C−D stretching vibration of partially deuterated ethane and/or the corresponding ethyl fragments appeared at approximately 2200 cm^{-1}. In the H−D exchange reaction of In-CHA(H_2) under a D_2 atmosphere monitored by in-situ FTIR, the band around 1720 cm^{-1} disappeared at 200 °C and the successive treatment with H_2 at 200 °C regenerated a similar band (Figure 16). Consumption of D_2 and generation of HD were also observed in the reaction of In-CHA(H_2) with D_2, when using a flow-type reactor with online mass spectrometry analysis. These results demonstrate the presence of In-hydrides in In-CHA.

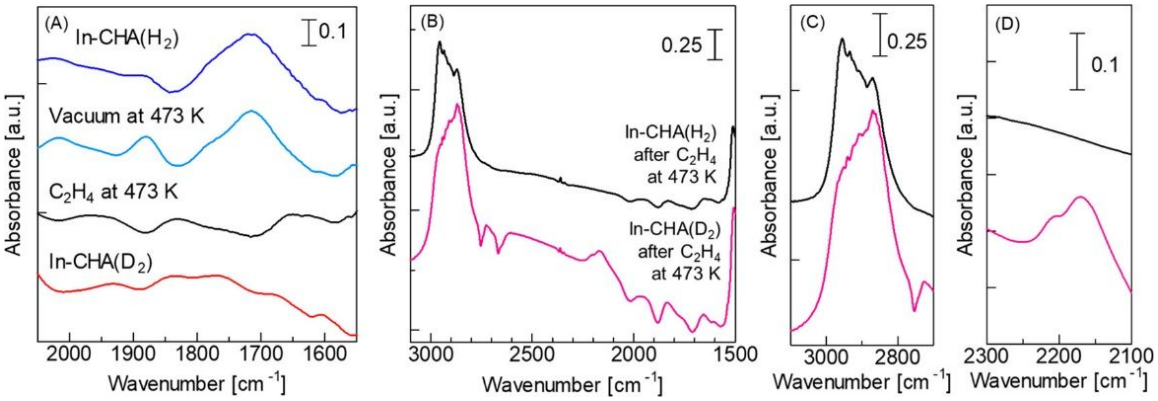

Figure 15. (A) FTIR spectra of In-CHA after treatment with H_2 at 500 °C (In-CHA(H_2)) followed by vacuum treatment or introduction of C_2H_4/He at 200 °C, and In-CHA after treatment with D_2 at 500 °C (In-CHA(D_2)). (B) Spectra after the introduction of C_2H_4/He at 200 °C for 20 min to In-CHA(H_2) and In-CHA(D_2). Enlarged views of (B) at approximately (C) 3100−2700 cm^{-1} and (D) 2300−2100 cm^{-1}. Reprinted with permission from ref 45. Copyright 2020 American Chemical Society.

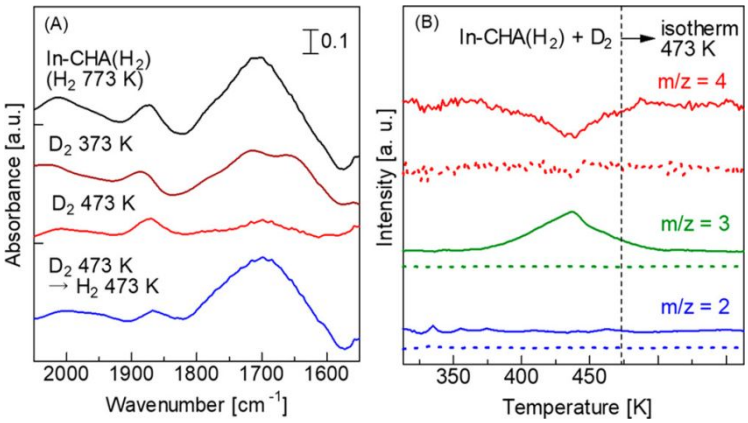

Figure 16. (A) FTIR spectra after H−D exchange reactions between In-CHA(H_2) and D_2 at 100 or 200 °C, as well as after the treatment of In-CHA used for the H−D exchange reaction with H_2 at 473 K. (B) Mass profiles for m/z = 2, 3, and 4 during the reaction between In-CHA(H_2) and D_2. The profiles for the control experiment using proton-type CHA (H-CHA) instead of In-CHA are indicated by dotted lines. Reprinted with permission from ref 45. Copyright 2020 American Chemical Society.

The detailed structure of In-hydrides was discussed by vibration analysis with a comparison of experimental results. The $[InH]^{2+}$ and $[InH_2]^{+}$ models at different paired Al sites were considered. The wavenumber of the In–H stretching vibration of $[InH]^{2+}$ is predicted to be approximately 1760–1800 cm^{-1}, whereas that of the asymmetric In–H stretching vibration of $[InH_2]^{+}$ ranged from 1721.1 to 1735.6 cm^{-1}. It was concluded that $[InH_2]^{+}$ was the main isolated In-hydrides in the CHA zeolite. TS calculations for the formation and decomposition of $[InH_2]^{+}$ were performed (Figure 17). The activation enthalpy for the decomposition of $[InH_2]^{+}$ to In^{+} was relatively high (approx. 260 kJ/mol), although $[InH_2]^{+}$ is thermodynamically less stable than In^{+}. $[InH_2]^{+}$ is kinetically wrapped by the zeolite cage, resulting in thermal stability of the isolated In-hydrides. Similar calculation results were obtained in the previous report by Bell et al.[97].

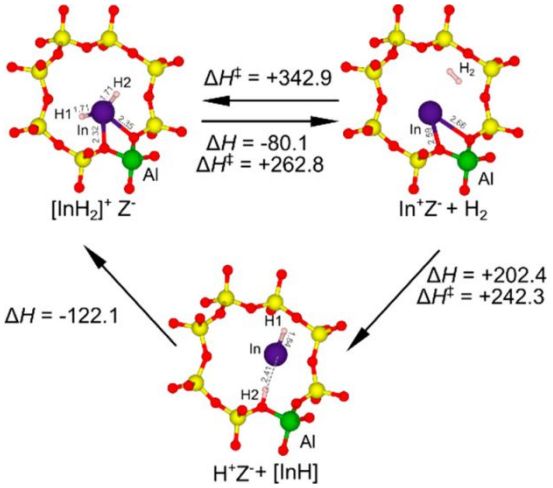

Figure 17. Optimized structure of the $[InH_2]^+$ ion $[AlO_4]^-$ site ($Z[InH_2]$) in the CHA zeolite and formation of $Z[InH_2]$ from Z[In] via direct and indirect pathways, as well as desorption of H_2 from $Z[InH_2]$. Activation enthalpies were estimated using TS calculations. Reprinted with permission from ref 45. Copyright 2020 American Chemical Society.

To explore the catalysis of In-hydrides in CHA zeolites, non-oxidative EDH was performed using several catalysts, including In-CHA, at 660 °C. In-CHA exhibited the high ethylene selectivity (> 96%) at ca. 26 % conversion with high carbon balance value (> 98%) (Figure 18). Notably, the initial conversion value did not decrease for at least 90 h, demonstrating the high durability of In-CHA. In contrast, Ga- and Zn-exchanged zeolites exhibited low to moderate ethylene selectivity (64–78%) and carbon balance value (62–82%), although the initial conversion values were higher (53–58%) than that of In-CHA. The conversion values quickly decreased within a few hours and reached below 26% after 20 h, indicating their low durability. A well-studied PtSn alloy catalyst ($PtSn/Al_2O_3$)[98] also decreased the conversion value by extending the reaction time to 90 h, resulting in the lower conversion value than that for In-CHA. The high selectivity of In-CHA was also demonstrated by the relationship between the conversion and selectivity of In-CHA, $PtSn/Al_2O_3$, and Ga-ZSM-5. Temperature-programmed oxidation (TPO) of the catalysts used for the 2 h reaction showed that coke formation occurred significantly for Ga- and Zn-exchanged zeolites and $PtSn/Al_2O_3$, whereas the peak derived from coke combustion was quite small for In-CHA. The high durability of In-CHA is ascribed to the suppression of coke formation. In-CHA selectively promoted EDH even under high-temperature conditions and was regenerable by O_2 treatment.

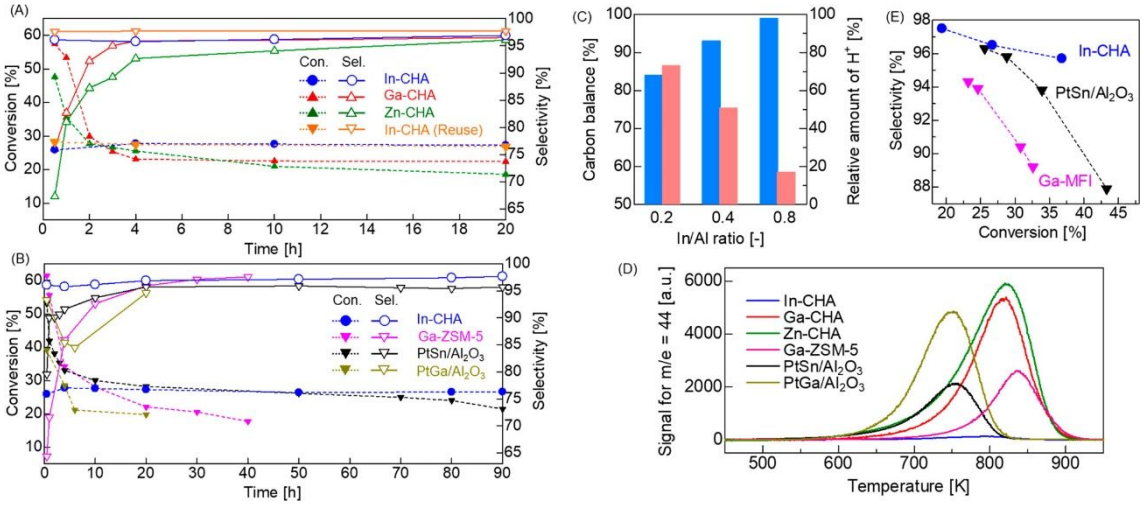

Figure 18. Time course of non-oxidative EDH using (A) In-, Ga-, and Zn-CHA for 20 h and (B) In-CHA, Al_2O_3-supported PtSn catalyst ($PtSn/Al_2O_3$) for 90 h, $PtGa/Al_2O_3$ for 20 h, and Ga-ZSM-5 for 40 h. (C) Effect of In/Al ratio on the carbon balance (blue) and relative number of Brønsted acid sites normalized to H-CHA (red). (D) TPO spectra of the catalysts used for the 2 h reaction. (E) Relationship between the conversion and selectivity for In-CHA, $PtSn/Al_2O_3$, and Ga-ZSM-5. Reprinted with permission from ref 45. Copyright 2020 American Chemical Society.

The most plausible active In species (In^+, $[InH]^{2+}$, and $[InH_2]^+$) for ethane dehydrogenation are discussed based on a combination of kinetic and theoretical studies (Figures 19 and 20). A previous study on Ga-exchanged zeolites reported by the group of Bell investigated the effects of H_2 partial pressure ($p(H_2)$) and Ga/Al ratio on the reaction rate in propane dehydrogenation[24]. A negative reaction order value (−0.1 to −0.3) was obtained, which was interpreted as the interconversion of more active $[GaH]^{2+}$ with H_2 to less active $[GaH_2]^+$ and H^+. The highest reaction rate normalized to the catalyst amount was observed at Ga/Al = 0.5, indicating that divalent $[GaH]^{2+}$ was the active site in the Ga-CHA tested in this study. Similar results were obtained for EDH using Ga-CHA. In contrast, In-CHA exhibits different kinetics. The zero-order reaction order with respect to $p(H_2)$ dependency was obtained while the reaction rate proportionally increased with the increase of In/Al from 0.4 to 0.8 (Figure 19A and C), indicating that monovalent In species, such as In^+ and $[InH_2]^+$, are more plausible rather than divalent $[InH]^{2+}$. The apparent activation enthalpy (ΔH) of EDH using In-CHA was determined to be 236 kJ/mol (Figure 19D). TS calculations of EDH over In-hydrides ($[InH]^{2+}$ or $[InH_2]^+$) and In^+ in different reaction mechanisms were investigated, and the highest ΔH values were compared. The highest ΔH in EDH over In-hydrides was calculated to be around 210–240 kJ/mol, except for the reaction over $[InH_2]^+$ in the σ-bond metathesis mechanism

(Figure 20), whereas the TS calculation of ethane dehydrogenation over In^+ in the alkyl mechanism resulted in the highest ΔH of 410 kJ/mol. Based on spectroscopic, kinetic, and theoretical results, $[InH_2]^+$ is the most plausible active site for ethane dehydrogenation. This is the first example of the formation and catalysis of isolated In-hydrides in zeolites.

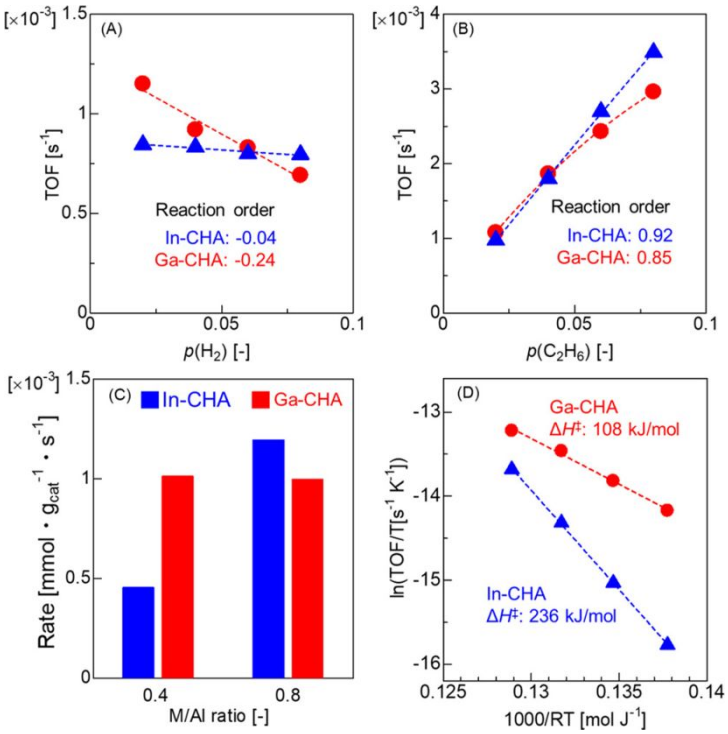

Figure 19. Kinetic studies of EDH using In-CHA (blue) and Ga-CHA (red). Comparison of TOF dependence of (A) $p(H_2)$ and (B) $p(C_2H_6)$. (C) Effect of M/Al ratio on the formation rate of ethylene. Conditions: 0.1 g of catalyst, 50 mL/min of H_2/C_2H_6/He, 600 °C for In, or 580 °C for Ga. (D) Eyring plot for ethane dehydrogenation (600–660 °C). The data for the kinetic studies were obtained under conditions yielding ethane conversions of <15%; the detailed conditions for each experiment are provided in the Supporting Information. Reprinted with permission from ref 45. Copyright 2020 American Chemical Society.

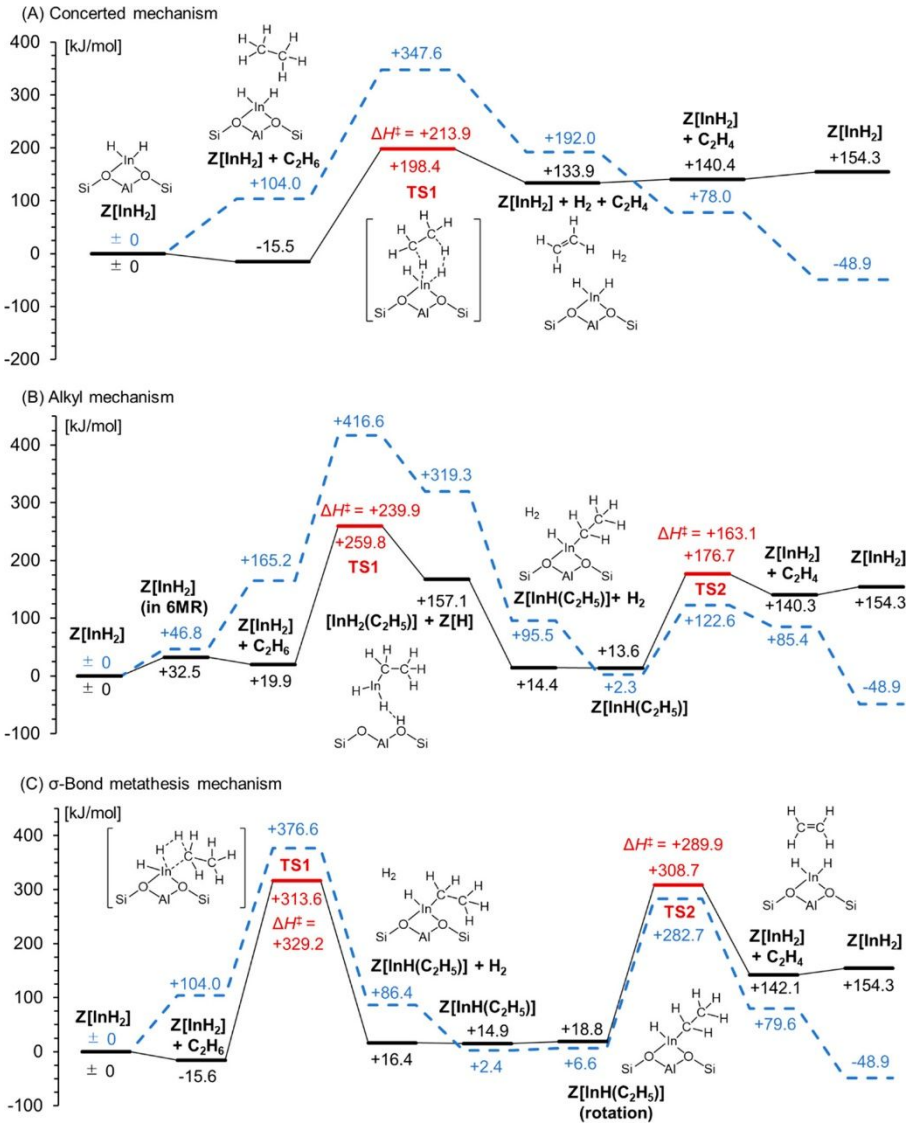

Figure 20. Enthalpy (solid lines) and free energy (dashed lines) profiles for ethane dehydrogenation over Z[InH_2] (A) via a concerted mechanism, (B) via an alkyl mechanism, and (C) via a σ-bond metathesis mechanism. Reprinted with permission from ref 45. Copyright 2020 American Chemical Society.

It is well known that surface Brønsted acid sites (BASs) induce coke formation via carbocation species, resulting in low selectivity and deactivation. The TS calculation of EDH over $[InH]^{2+}$ ions indicated that BASs or carbocations were formed by the C-H cleavage of C_2H_6 as relatively stable species. In contrast, EDH over $[InH_2]^+$ ions does not involve the *in-situ* generation of BASs as stable intermediates, suggesting that the abundance of *in-situ* generated BASs or carbocations in EDH over $[InH_2]^+$ ions is less than that over $[InH]^{2+}$ ions. The TS calculation for EDH by Ga-zeolites from Bell's group also indicated a similar

difference in the reaction mechanisms between $[GaH]^{2+}$ and $[GaH_2]^{+}$ ions[97] The difference in the local structure of active metal hydrides, dihydrides, or monohydrides resulted in the suppression of coke formation as well as superior selectivity and durability of In-CHA.

5. Control of Ga-hydride formation in MFI zeolites for selective EDH [47]

As described in the previous section, we observed the formation of isolated In-hydrides in the form of $[InH_2]^{+}$ by high-temperature H_2 treatment of In-exchanged CHA zeolite (In-CHA) prepared via the RSSIE reaction. Although In-CHA exhibited higher selectivity and durability for EDH than Ga-CHA, the apparent activation barrier for Ga-CHA was much lower than that for In-CHA. We envisioned that $[GaH_2]^{+}$ ions would be reasonable active sites that exhibit higher activity than $[InH_2]^{+}$ ions and higher selectivity than $[GaH]^{2+}$ ions, leading to the development of effective Ga-zeolite catalysts for EDH.

The preferential formation of $[GaH_2]^{+}$ ions over $[GaH]^{2+}$ ions is theoretically induced by increasing the Ga loading amount at Ga/Al = 1.0, because monovalent Ga ions can be stabilized by one Al site, whereas divalent Ga ions can be formed only on paired Al sites. Even though the formation of inactive Ga^{+} cations is also induced, Ga^{+} cations likely act as spectators to suppress coke formation by replacing BASs with charge-compensating cations (Figure 21). In this study, we found the high-loading Ga-MFI (Ga/Al = 1.0) treated at a high temperature of 800 °C (Ga-MFI-1.0(800)) afforded $[GaH_2]^{+}$ ions as the major Ga-hydride whereas $[GaH]^{2+}$ ions were preferentially formed in the low-loading Ga-MFI (Ga/Al = 0.3) treated with H_2 at a conventional temperature of 550 °C (Ga-MFI-0.3(550)). In EDH, Ga-MFI-1.0(800) exhibited much higher selectivity owing to much less coke formation compared to low- and medium-loading Ga-MFI, indicating that $[GaH_2]^{+}$ ions likely serve as selective and coke-resistant active sites for EDH. Although most previous studies have focused on the characterization and dehydrogenation catalysis of low- to medium-loading Ga-MFIs[23–26,99,100], studies on Ga-MFIs with high Ga loading (Ga/Al = ca. 1.0) have been limited[22,101].

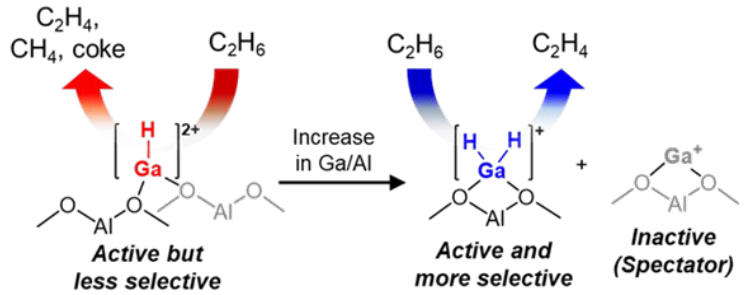

Figure 21. The formation of isolated Ga-hydrides in MFI controlled by increasing the Ga loading toward selective EDH.

First, we investigated the effects of the Ga loading amount (Ga/Al) and H_2 treatment temperature on the RSSIE to control the formation of Ga-hydrides (Figure 22). The IR spectrum for Ga-MFI prepared under the conditions (Ga/Al = 0.3 and treated with H_2 at 550 °C, denoted as Ga-MFI-0.3(550)) exhibited a stronger peak around 2060 cm^{-1} with a weaker peak around 2040 cm^{-1}. These peaks are assignable to the Ga−H stretching vibration of $[GaH]^{2+}$ and $[GaH_2]^{+}$, respectively[24]. With increasing Ga loading amount (from Ga/Al = 0.3, 0.5, and 1.0) and the temperature of the H_2 treatment (from 550 to 700 °C and 800 °C), the peak intensity corresponding to $[GaH]^{2+}$ decreased and that corresponding to $[GaH_2]^{+}$ increased. The main formation of $[GaH_2]^{+}$ was observed over Ga-MFI-1.0(800), prepared with Ga/Al = 1.0, and H_2 treatment at 800 °C. The other Ga species and remaining Brønsted acid sites (BASs) were also characterized by *in-situ* FTIR spectroscopy using pyridine and NH_3 as probe molecules, respectively. The unreacted GaOx species and BASs were considerably remained for Ga-MFI-0.3(550). For Ga-MFI-1.0(800), a strong peak derived from Ga^{+} was observed, while the peaks corresponding to GaOx and BASs were much smaller than those of the other Ga-MFIs. The high Ga loading amount and high-temperature H_2 treatment are favorable not only for the main formation of $[GaH_2]^{+}$ but also for decreasing the number of remaining BASs.

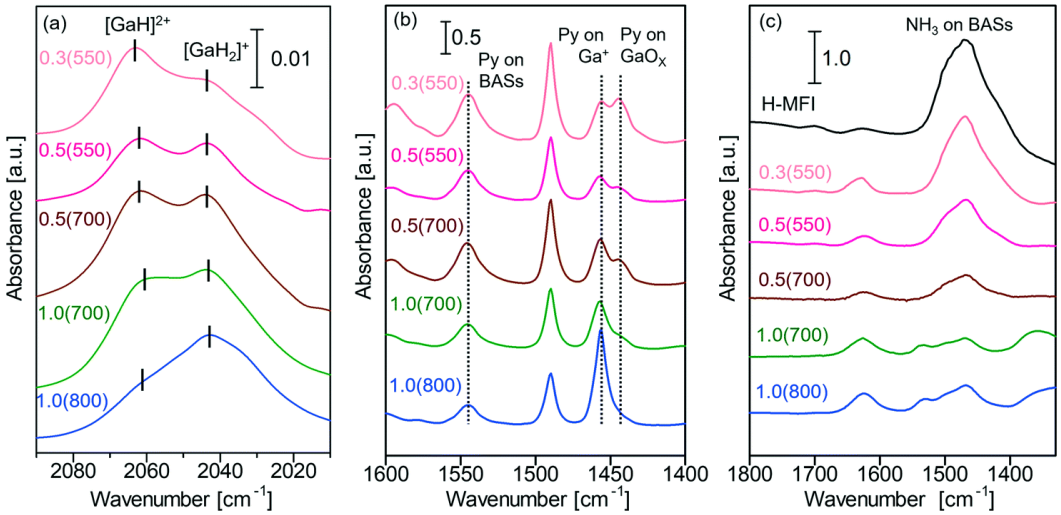

Figure 22. Characterization of Ga species in Ga-MFI-X(Y) (X: Ga/Al ratio, Y: H_2 treatment temperature). (a) Difference in FTIR spectra at 50 °C without exposure to air. (b) FTIR spectra of the adsorbed pyridine (Py) species at 150 °C. (c) IR spectra of the adsorbed NH_3 species at 50 °C. For (b) and (c), the spectra were recorded after the saturation of Py or NH_3 adsorption followed by He purging.

A series of Ga-MFIs was applied to EDH, and their catalytic performances were compared (Figure 23a). Although a few studies on EDH using Ga-MFIs have been reported, the

catalysts were prepared with low-to-medium Ga/Al values. Alkane dehydrogenation using high-loading Ga-MFIs has rarely been investigated. Ga-MFI-0.3(550) showed a relatively high initial conversion (78%), whereas both the ethylene selectivity and carbon balance values were very low (55% and 34%, respectively). The activity rapidly decreased within a few hours, and the conversion value at 15 h was 18%. The Ga-MFIs prepared with higher Ga/Al and higher temperature H_2 treatment exhibited better ethylene selectivity and carbon balance values, achieving superior durability, although the initial conversion value decreased. The highest durability was achieved using Ga-MFI-1.0(800), where good ethylene selectivity and carbon balance values were observed. Notably, the developed Ga-MFI-1.0(800) was applicable under high-concentration conditions (50%), where a good conversion value and high ethylene selectivity were maintained for at least 30 h. The ethylene formation rate reached 72.1 mmol g^{-1} h^{-1}, which was the highest value among the reported Pt-free catalysts (Table 1).[102] The comparison of catalytic performance with representative reported catalyst system is summarized in Table 1.

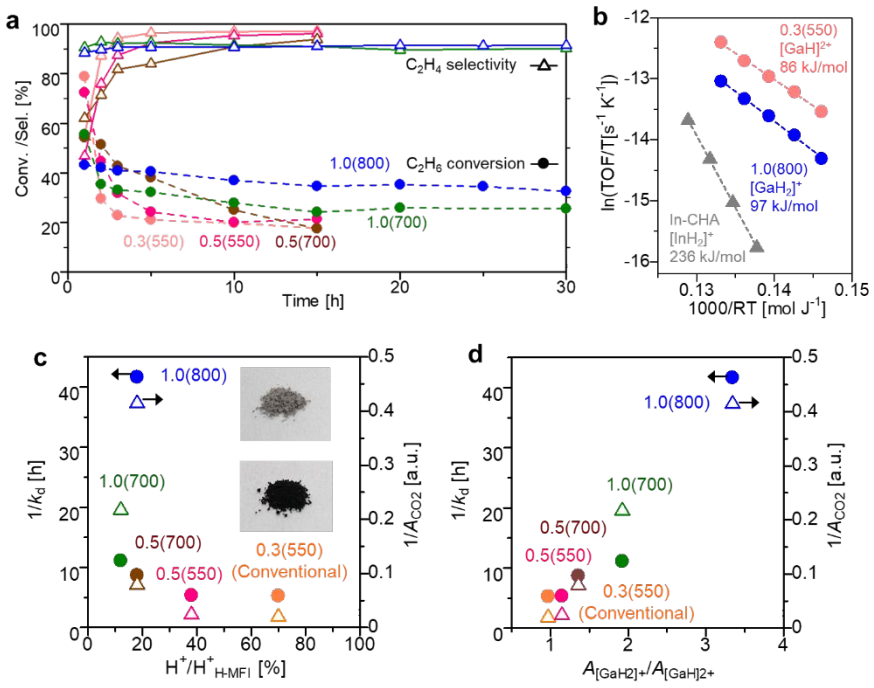

Figure 23. (a) Conversion and selectivity of EDH using Ga-MFI-X(Y). Reaction conditions: 100 mg of Ga-MFI-X(Y), 10 mL/min of 10% C_2H_6/He, 660 °C. (b) TPO profiles of a series of Ga-MFI after reaction for 2 h. (c) Plots of reciprocals of k_d in dehydrogenation tests and A_{CO2} in TPO experiments (indices of durability and coking suppression, respectively) as a function of the relative amount of the remaining BASs based ($H^+/H^+_{H\text{-}MFI}$). The upper and lower inset pictures are Ga-MFI-1.0(800) and 0.3(550), respectively, after 2 h of reaction. (d) Plots of reciprocals of k_d and A_{CO2} as a function of $A_{[GaH2]+}/A_{[GaH]2+}$.

Table 1. Comparison of conversion, selectivity, and deactivation rate of Ga-MFI and representative reported Pt-free catalysts in non-oxidative EDH.

Catalyst	Temp. [°C]	Cat. [mg]	Flow [mL/min]	C_2H_6 Conc. [%]	C_2H_6 Conv. [%]	C_2H_4 Sel. [%]	C_2H_4 Formation Rate [mmol/(g·h)]	Deactivation Rate (k_d) [h^{-1}]	Ref.
Ga-MFI-1.0(800)	660	100	10	10	43.1	89.7	10.4	0.024 (15 h)	[47]
	660	50	10	50	28.5	92.6	72.1	0.014 (30 h)	[47]
Ga-MFI-0.3(550)	660	100	10	10	79.1	55.0	11.7	0.190 (15 h)	[47]
In-CHA	700	100	7.5	13	37.4	95.1	9.2	0.0025 (20 h)	[45]
Cr0.8MFI	650	100	10	10	36.2	> 99	19.2	0.0046 (40 h)	[103]
Fe-containing MFI siliceous zeolite	600	200	6.6	30	26.3	97.5	10.4	n.a.	[104]
0.10Ba-Ga-α-Al_2O_3	700	100	143	12.6	1	98	4.7	n.a.	[105]
FeZSM5	600	100	60	9	28	71.6	29.0	0.071 (4.5 h)	[106]
Ga/SiO_2-doped TiO_2	650	200	30	3	46.0	84.9	4.7	0.81 (6 h)	[107]
5Cr/MCM-41E	650	160	50	15	23	99	28.6	n.a.	[108]
Co-MFI	650	200	30	3	54.5	87.8	5.8	0.078 (6 h)	[109]
Ni_3Ga/Al_2O_3	600	100	20	10	10.0	94.0	5.0	0.018 (30 h)	[110]
Pd-In-0.8/SiO_2	600	200	50	5	24.0	>99	8.0	0.090 (3 h)	[111]
6% Co@MFI	600	300	30	90	16.2	99	38.6	n.a.	[112]

In our previous study, we investigated the relationship between durability, coke formation, and the remaining BASs; however, the influences of $[GaH_2]^+/[GaH]^{2+}$ formation at different ratios on catalytic performance were not systematically studied. In this Perspective, the formation ratio of $[GaH_2]^+/[GaH]^{2+}$ was estimated by the peak area of the FTIR measurement, including peak deconvolution ($A_{[GaH2]+}/A_{[GaH]2+}$), and its relationship with coke formation and durability was examined. The reciprocals of the deactivation rate ($1/k_d$) and relative CO_2 peak

area ($1/A_{CO2}$) obtained from TPO were used as indices of the durability and suppression of coke formation. These two indices were plotted as a function of the remaining BASs ($H^+/H^+_{H\text{-}MFI}$) and the formation ratio of $[GaH_2]^+$, $A_{[GaH2]+}/A_{[GaH]2+}$ (Figure 23c and d). For low-to-medium-loading amount Ga-MFIs, 0.3(550), 0.5(550), and 0.5(700), showed higher $1/k_d$ and $1/A_{CO2}$ values with the decrease of $H^+/H^+_{H\text{-}MFI}$. However, in the case of high-loading Ga-MFIs, 1,0(700) and 1.0(800), coke formation was suppressed and better durability was achieved for Ga-MFI-1.0(800) despite the similarity ($H^+/H^+_{H\text{-}MFI}$). In the plot of as a function of $A_{[GaH2]+}/A_{[GaH]2+}$, both $1/k_d$ and $1/A_{CO2}$ monotonically increased with an increase in $A_{[GaH2]+}/A_{[GaH]2+}$. These results show that the different formation ratios of isolated Ga-hydrides influence coke formation, affecting durability. The high durability and coke-resistance of Ga-MFI-1.0(800) were ascribed to not only the low remaining BASs but also the main formation of $[GaH_2]^+$. The Eyring plots for EDH were further compared for Ga-MFI-1.0(800), 0.3(550), and In-CHA as catalysts with different active isolated hydrides, $[GaH_2]^+$, $[GaH]^{2+}$, and $[InH_2]^+$, respectively (Figure 23b). The experimental ΔH value of Ga-MFI-1.0(800) was determined to be 97 kJ/mol, which is similar to that of Ga-MFI-0.3(550) (86 kJ/mol) and much lower than that of In-CHA (236 kJ/mol). The lower activation energy of Ga-exchanged zeolites than that of In-exchanged zeolites in EDH was also reported by Lobo[113] The combined results suggest that $[GaH_2]^+$ is a reasonably active Ga-hydrides showing both high activity and selectivity for the EDH reaction.

6. Formation and catalysis of isolated In- and Ga-hydrides in different zeolite frameworks [48,49]

In the development of zeolite-based catalysts, the framework type often affects the formation of active metal cation species, resulting in different catalytic performances. Although a few examples of isolated metal hydrides in zeolites have been reported (vide infra), the effect of the zeolite framework type on formation and catalysis has not yet been investigated. As our continuous studies, we further investigated the formation and catalysis of isolated In- and Ga-hydrides in other zeolites for EDH reaction[48,49].

For In-exchanged zeolites[48], In-MFI (10-membered rings), BEA, and MOR (12-membered rings) were examined for comparison with CHA (8-membered ring). Note that their SiO_2/Al_2O_3 ratios are similar (20.0 to 25.0) and RSSIE was conducted with the same In loading amount (In/Al = 0.8). In the EDH reaction, In-CHA uniquely showed higher activity compared to other In-exchanged zeolites, although high ethylene selectivity was obtained for all In-CHA zeolites (Figure 24). The Eyring plots revealed that ΔH in EDH using In-MFI, BEA, and MOR ranged from 300–364 to kJ/mol, which was much higher than that in EDH using In-CHA. A CHA zeolite with a higher Al content (SiO_2/Al_2O_3 = 13.7) was also used to prepare the

corresponding In-CHA (In-CHA(Al-rich), In/Al = 0.8). In-CHA(Al-rich) exhibited a higher conversion value than In-CHA, whereas ΔH was similar to that of In-CHA (258 kJ/mol and 236 kJ/mol). In-*situ* FTIR spectroscopy of In-CHA(Al-rich) revealed the formation of In-hydrides. Active In-hydride species are likely to be formed only in CHA zeolites, resulting in the superior activity of In-CHA and In-CHA(Al-rich) to other In-exchanged zeolites. To discuss this, H–D exchange reactions were additionally conducted for In-MFI and In-MOR (Figure 25). As described above, in the case of In-CHA, the In-hydrides generated after H_2 treatment at 500 °C reacted with D_2 (m/z = 4) to afford HD (m/z =3) as a product of H–D exchange reactions. When the reaction of H_2-treated In-MFI and In-MOR under D_2 flow was investigated, any consumption of D_2 and formation of HD formation were not observed under the same reaction temperatures. These results prove the absence of active In-hydrides in In-MFI and In-MOR, supporting the interpretation of the effect of zeolite framework type on the EDH catalysis of In-exchanged zeolites.

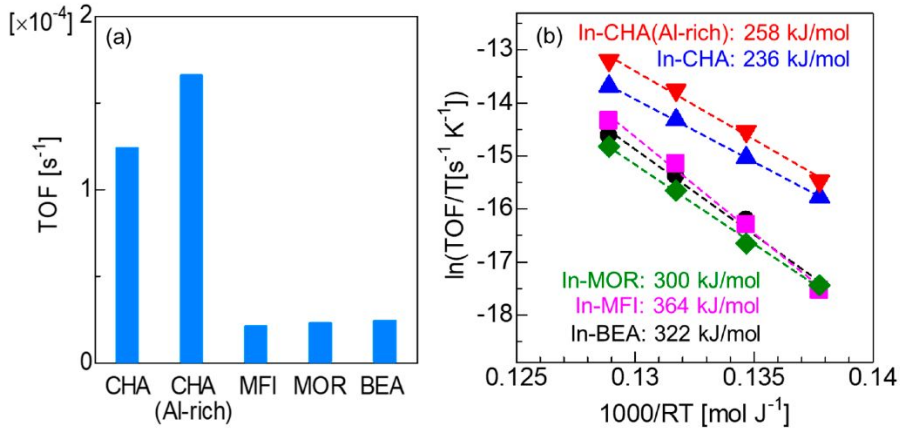

Figure 24. (a) Effect of zeolite host on turnover frequency (TOF) normalized to the amount of In obtained at 600 °C. (b) Eyring plots and apparent activation enthalpies for ethane dehydrogenation (600–660 °C) using In-MFI (pink), In-MOR (green), In-BEA (black), and In-CHA(Al-rich) (red). The plots were obtained under ethane conversion below 15%.

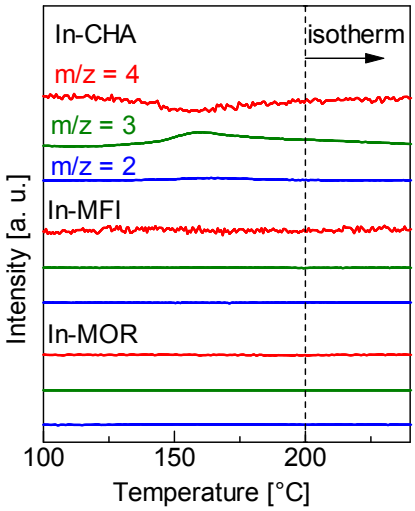

Figure 25. Mass profiles for m/z = 2, 3, and 4 during the reaction between In-exchanged zeolites (In-CHA, MFI, and MOR) and D_2.

In the context of Ga-exchanged zeolites[49], low- and high-loading Ga-exchanged MOR and CHA zeolites (Ga-MOR and -CHA) were prepared under identical conditions (Ga/Al = 0.3, H_2 at 550 °C, and Ga/Al = 1.0, with H_2 at 800 °C, denoted as 0.3(550) and 1.0(800), respectively) and then compared with Ga-MFIs. The peak was hardly observed around 2050 cm^{-1} in IR spectrum for Ga-CHA-0.3(550). With an increase in the Ga/Al ratio and H_2 treatment temperature (Ga-CHA-1.0(800)), a peak at 2050 cm^{-1}, assignable to the Ga–H stretching vibration, was observed. In the case of Ga-MOR, two peaks at 2077 and 2050 cm^{-1} were observed for Ga-MOR-0.3(550), possibly assignable to $[GaH]^{2+}$ and $[GaH_2]^{+}$, respectively, whereas a main peak corresponding to $[GaH_2]^{+}$ was detected at 2050 cm^{-1} with a much higher intensity compared to Ga-CHA-1.0(800). In the EDH reaction, Ga-MOR-1.0(800) exhibited good ethylene selectivity and durability, although the conversion value was lower than that of Ga-MFI-1.0(800), as discussed above. In contrast, the activity of other Ga-CHA and -MOR decreased with the extending the reaction time, and the conversion values were lower than that for Ga-MOR-1.0(800). To understand the effects of the zeolite framework types and preparation conditions, the relative amounts of active Ga-hydrides were estimated by the H–D exchange reaction monitored with *in-situ* FTIR spectroscopy. The steady-state ethylene yield at 3 h as an index of activity was plotted as a function of the intensity of the negative band around 2050 cm^{-1} (Figure 26). A linear relationship was obtained where both the activity and the relative amount of active Ga-hydrides increased in the following order: Ga-CHA-0.3(550) < Ga-CHA-1.0(800) < Ga-MOR-0.3(550) < Ga-MOR-1.0(800) < Ga-MFI-1.0(800). The kinetic study of EDH using Ga-CHA-1.0(800) and Ga-MOR-1.0(800) was also

examined. Although the ΔH values were similar among the tested catalysts, the reaction order of C_2H_6 partial pressure for Ga-CHA-1.0(800) was lower than those for Ga-MFI-1.0(800) and Ga-MOR-1.0(800) (Figure 27). These results demonstrate that isolated Ga-hydrides are responsible for the EDH reaction, regardless of the different zeolite framework types and kinetics/mechanisms.

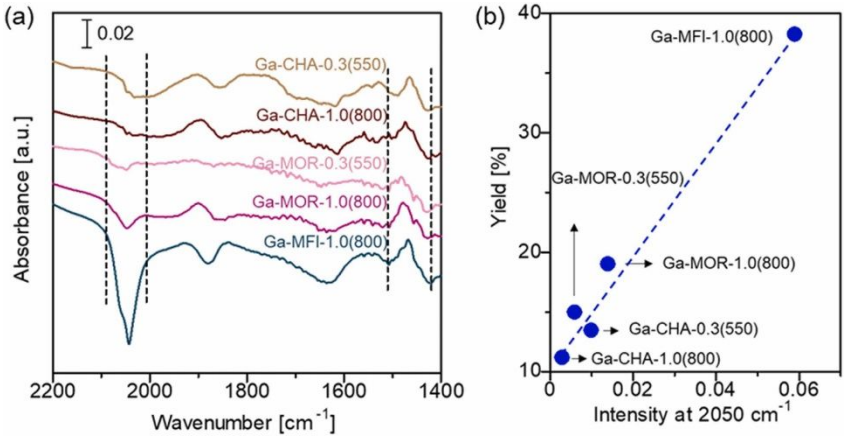

Figure 26. (a) FTIR spectra of the H–D exchange experiments in Ga-CHA, MOR, and MFI-1.0(800) at 50 °C. The catalysts were treated with D_2 at 400 °C for 15 min after the H_2 treatment at 800 °C. (b) Plot of ethylene yield at 3 h in ethane dehydrogenation tests and intensity at 2050 cm^{-1} as a function of the amount of Ga-hydrides. Reprinted with permission from ref 49. Copyright 2022 Elsevier.

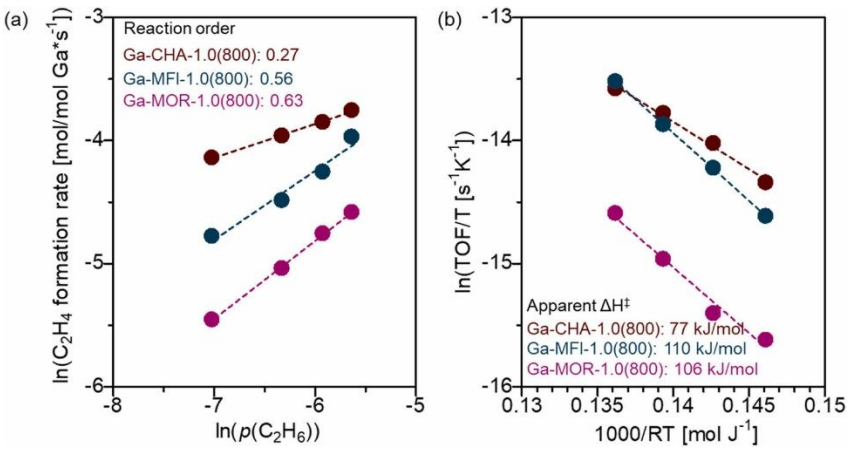

Figure 27. Kinetic study for C_2H_6 dehydrogenation by using Ga-CHA-1.0(800) and Ga-MOR-1.0(800). Dependence of C_2H_4 formation rate on (a) $p(C_2H_6)$ and (b) reaction temperature. Reaction conditions: 100 mg of catalyst, (a) 50 mL/min of 2–8% C_2H_6/He, and 600 °C. (b) 50 mL/min of 4% C_2H_6/He, 550–610 °C. Reprinted with permission from ref 49. Copyright 2022 Elsevier.

Conclusions and Outlook

In this Perspective, we described our continuous study of In- and Ga-exchanged zeolites for CH_4 and C_2H_6 transformations. For the preparation of In- and Ga-exchanged CHA, the RRSIE reaction for Ga_2O_3/CHA required a higher temperature to promote the exchange reaction considerably (above 700 °C) than the RSSIE reaction for In_2O_3/CHA. The O_2 treatment of In- and Ga-CHA resulted in the formation of the corresponding metal–oxo clusters, as indicated by XAS spectroscopy. Both InO_X-CHA and GaO_X-CHA (O_2-treated In- and Ga-CHA) were active for POM at room temperature to produce surface-adsorbed oxygenates. Adsorbed formic acid species were formed over InO_X-CHA, whereas surface dioxymethylene species (-OCH_2O-, adsorbed formaldehyde species) were detected over GaO_X-CHA. The active In- and Ga-oxo clusters were discussed based on *ab initio* thermodynamics and TS calculations. In both cases, paired Al sites in 8MR were more favorable for the formation of clusters than those in 6MR. Among the considered models, $[In_2O_2]^{2+}$ and $[Ga_2O(OH)_2]^{2+}$ showed the lowest activation barrier values (approx. 90 and 100 kJ/mol), respectively, which are reasonable for CH_4 activation at room temperature. The different product selectivity in POM (formic acid species for In-CHA and formaldehyde species for Ga-CHA) is interpreted as the distinction of the lowest activation barrier values between $[In_2O_2]^{2+}$ and $[Ga_2O(OH)_2]^{2+}$.

We also found that isolated In-hydrides were formed in CHA zeolites after RSSIE. Active In-hydrides were uniquely formed in In-exchanged CHA, whereas the use of other zeolites such as MOR and MFI did not afford active In-hydrides. Detailed characterization with the aid of vibration analysis indicated that $[InH_2]^+$ ions are plausible In-hydrides, as opposed to $[InH]^{2+}$ ions. DFT calculations indicated that $[InH_2]^+$ is kinetically trapped by the zeolite cage, suppressing decomposition under high-temperature conditions, although In^+ is thermodynamically more stable than $[InH_2]^+$. In the case of Ga-MFIs, both $[GaH_2]^+$ and $[GaH]^{2+}$ were formed, and their formation ratio depended on the preparation conditions, such as the loading amount (Ga/Al ratio) and H_2 temperature in the RSSIE. Conventional Ga-MFIs, prepared under relatively low Ga loading and low temperature, possess $[GaH]^{2+}$ ions as the dominant Ga-hydrides. High Ga loading and high-temperature conditions are favorable for the formation of monovalent $[GaH_2]^+$, although Ga^+ is also formed. The relative number of Ga-hydrides, as determined by FTIR and H–D exchange reactions, differs among the different zeolite frameworks under similar preparation conditions.

In the context of the catalysis of isolated In- and Ga-hydrides, In-CHA with $[InH_2]^+$ selectivity promoted EDH and exhibited high durability, where the initial conversion value was maintained in long-term reactions. The combined results of spectroscopic, kinetic, and theoretical studies revealed that $[InH_2]^+$ ions are the most plausible active sites among the

reduced In species (In^+ cations and isolated In-hydrides). Other In-exchanged zeolites also showed high C_2H_4 selectivity, although the apparent activation enthalpy was much higher than that for In-CHA. This is ascribed to the presence or absence of In-hydrides, supporting the idea that isolated In-hydrides are active sites for EDH. In the context of Ga-zeolites, Ga-CHA and conventional Ga-MFIs showed low selectivity and durability, although the initial conversion value was higher than that of In-CHA. TS calculations suggest that the local structures of isolated In- and Ga-hydrides were closely related to C_2H_4 selectivity and durability. The C–H bond cleavage of ethane over $[MH]^{2+}$ (M = In and Ga) ions may induce the generation of BASs and/or carbocations as relatively stable intermediates, which may promote coke formation, whereas $[MH_2]^+$ ions can activate the C–H bond of C_2H_6 without the formation of BASs or carbocations. The higher selectivity of In-CHA compared to conventional Ga-MFIs is ascribed to the difference in the abundance of *in-situ* generated BASs and/or carbocations. Based on this insight, we investigated the EDH catalysis of high-loading Ga-MFIs with $[GaH_2]^+$ as the dominant Ga-hydride. The optimized Ga-MFI (Ga-MFI-1.0(800)) promoted EDH with relatively good selectivity and durability. The highest C_2H_4 formation rate among previously reported Pt-free catalysts was also achieved at high C_2H_6 concentrations. A study on the relationship between catalyst durability and the formation ratio of $[GaH_2]^+/[GaH]^{2+}$ over a series of Ga-MFIs revealed that a catalyst with a higher $[GaH_2]^+/[GaH]^{2+}$ ratio showed better durability. The distinction in the steady-state EDH activity of Ga-exchanged zeolites with different frameworks was interpreted as the relative amounts of active Ga-hydrides for the H–D exchange reaction. These findings indicate that isolated In and Ga-hydrides are active for EDH, and the local structure of hydride species is key to obtaining high selectivity. The advantage of In-exchanged zeolites over Ga-exchanged ones is high ethylene selectivity and low coke formation owing to the exclusive formation of $[InH_2]^+$, leading to long-term durability. Despite the difficulty in controlling the formation of $[GaH_2]^+/[GaH]^{2+}$, Ga-exchanged zeolites are more promising than In-exchanged ones from the viewpoint of activity.

The catalysis of typical metal groups has been less explored than that of transition metal groups. Our recent results demonstrate the catalytic potential of typical metal-exchanged zeolites for alkane transformations. In addition, Zn-exchanged zeolites have been studied for light-alkane activations/transformations by several research groups, where oxidized and reduced Zn species have been proposed as the active sites[92–94,114–116]. The advantage of Ga- and In-exchanged zeolites over other metal-exchanged ones is the stability of reduced cationic species in the presence of H_2 under high temperature conditions (i,e, difficulty of reduction of cationic species to metallic ones). This enables the preparation of high loading materials by RSSIE, which possibly reduces the remaining Bronsted acid sites, resulting in

the suppression of coke formation and long-term durability. Many challenges remain, including the synthesis of other types of metal-exchanged zeolites and how different zeolite frameworks affect the formation of active metal species. To control the local structure of active metal species, the regulation of Al sites in zeolites is also desirable[117–120]. From a mechanistic perspective, *operando* spectroscopic studies should be conducted to detect active metal hydrides under real operating conditions and to reveal experimentally reveal how alkane molecules are activated are formidable tasks.

Conflicts of interest

There are no conflicts to declare.

Acknowledgments

The preparation of this Perspective and the studies were supported by KAKENHI (Grant No. JP20H02518, JP20H02775, and JP21H04626) from the Japan Society for the Promotion of Science (JSPS), KAKENHI on Innovative Areas “Hydrogenomics” (JP21H00012), the JST-CREST project JPMJCR17J3, and the JST-SPRING project JPMJSP2119. These studies were also supported by the Joint Usage/Research Center for Catalysis (Hokkaido University), the ENEOS Tonen General Research/Development Encouragement & Scholarship Foundation, and the “Grant for Research” of The Japan Petroleum Institute. S. Y. acknowledges Grant-in-Aid for JSPS Fellows (DC2). Part of the calculations were conducted on supercomputers at RIIT (Kyushu Univ.) and ACCMS (Kyoto University).

References

1 E. T. C. Vogt and B. M. Weckhuysen, *Chem Soc Rev*, 2015, **44**, 7342–7370.

2 C. Wei, Q. Yu, J. Li and Z. Liu, *ACS Catal*, 2020, **10**, 4171–4180.

3 J. Zhong, J. Han, Y. Wei, P. Tian, X. Guo, C. Song and Z. Liu, *Catal Sci Technol*, 2017, **7**, 4905–4923.

4 P. Tian, Y. Wei, M. Ye and Z. Liu, *ACS Catal*, 2015, **5**, 1922–1938.

5 U. Olsbye, S. Svelle, M. Bjørgen, P. Beato, T. V. W. Janssens, F. Joensen, S. Bordiga and K. P. Lillerud, *Angew Chem Int Ed*, 2012, **51**, 5810–5831.

6 M. Ye, P. Tian and Z. Liu, *Engineering*, 2021, **7**, 17–21.

7 J. Lee, J. R. Theis and E. A. Kyriakidou, *Appl Catal B*, 2019, **243**, 397–414.

8 K. Khivantsev, N. R. Jaegers, L. Kovarik, S. Prodinger, M. A. Derewinski, Y. Wang, F. Gao and J. Szanyi, *Appl Catal A Gen*, 2019, **569**, 141–148.

9 J. Wang, H. Zhao, G. Haller and Y. Li, *Appl Catal B*, 2017, **202**, 346–354.

10 F. Gao, J. H. Kwak, J. Szanyi and C. H. F. Peden, *Top Catal*, 2013, **56**, 1441–1459.

11 A. M. Beale, F. Gao, I. Lezcano-Gonzalez, C. H. F. Peden and J. Szanyi, *Chem Soc Rev*, 2015, **44**, 7371–7405.

12 D. W. Fickel, E. D'Addio, J. A. Lauterbach and R. F. Lobo, *Appl Catal B*, 2011, **102**, 441–448.

13 Q. Zhang, S. Gao and J. Yu, *Chem Rev*, , DOI:10.1021/acs.chemrev.2c00315.

14 J. Lee, J. R. Theis and E. A. Kyriakidou, *Appl Catal B*, 2019, **243**, 397–414.

15 Z.-P. Hu, J. Han, Y. Wei and Z. Liu, *ACS Catal*, 2022, **12**, 5060–5076.

16 Y. Ono, *Catalysis Reviews*, 1992, **34**, 179–226.

17 N. Y. Chen and T. Y. Yan, *Ind Eng Chem*, 1986, **25**, 151–155.

18 D. Seddon, *Catal Today*, 1990, **6**, 351–372.

19 H. Kitagawa, Y. Sendoda and Y. Ono, *J Catal*, 1986, **101**, 12–18.

20 K. M. Dooley, C. Chang and G. L. Price, *Appl Catal A Gen*, 1992, **84**, 17–30.

21 G. D. Meitzner, E. Iglesia, J. E. Baumgartner and E. S. Huang, *J Catal*, 1993, **140**, 209–225.

22 V. B. Kazansky, I. R. Subbotina, R. A. van Santen and E. J. M. Hensen, *J Catal*, 2004, **227**, 263–269.

23 N. M. Phadke, J. van der Mynsbrugge, E. Mansoor, A. B. Getsoian, M. Head-Gordon and A. T. Bell, *ACS Catal*, 2018, **8**, 6106–6126.

24 N. M. Phadke, E. Mansoor, M. Bondil, M. Head-Gordon and A. T. Bell, *J Am Chem Soc*, 2019, **141**, 1614–1627.

25 M. W. Schreiber, C. P. Plaisance, M. Baumgärtl, K. Reuter, A. Jentys, R. Bermejo-Deval and J. A. Lercher, *J Am Chem Soc*, 2018, **140**, 4849–4859.

26 N. M. Phadke, E. Mansoor, M. Head-Gordon and A. T. Bell, *ACS Catal*, 2021, **11**, 2062–2075.

27 Y. Yuan, J. S. Lee and R. F. Lobo, *J Am Chem Soc*, 2022, **144**, 15079–15092.

28 L. Ni, R. Khare, R. Bermejo-Deval, R. Zhao, L. Tao, Y. Liu and J. A. Lercher, *J Am Chem Soc*, 2022, **144**, 12347–12356.

29 E. J. M. Hensen, E. A. Pidko, N. Rane and R. A. van Santen, *Angew Chem Int Ed*, 2007, **46**, 7273–7276.

30 E. A. Pidko, R. A. van Santen and E. J. M. Hensen, *Phys Chem Chem Phys*, 2009, **11**, 2893–2902.

31 E. Mansoor, M. Head-Gordon and A. T. Bell, *ACS Catal*, 2018, **8**, 6146–6162.

32 Y. V Joshi and K. T. Thomson, *Catal Today*, 2005, **105**, 106–121.

33 M. S. Pereira and M. A. C. Nascimento, *Chem Phys Lett*, 2005, **406**, 446–451.

34 E. A. Pidko, R. A. van Santen and E. J. M. Hensen, *Phys Chem Chem Phys*, 2009, **11**, 2893–2902.

35 E. A. Pidko, V. B. Kazansky, E. J. M. Hensen and R. A. van Santen, *J Catal*, 2006, **240**, 73–84.

36 H. Solt, F. Lónyi, R. M. Mihályi, J. Valyon, L. B. Gutierrez and E. E. Miro, *J Phys Chem C*, 2008, **112**, 19423–19430.

37 G. L. Price, V. Kanazirev, K. M. Dooley and V. I. Hart, *J Catal*, 1998, **173**, 17–27.

38 V. I. Hart, M. B. Bryant, L. G. Butler, X. Wu and K. M. Dooley, *Catal Lett*, 1998, **53**, 111–118.

39 T. Baba, Y. Abe, K. Nomoto, K. Inazu, T. Echizen, A. Ishikawa and K. Murai, *J Phys Chem B*, 2005, **109**, 4263–4268.

40 E. Kikuchi and M. Ogura, *Catalysis Surveys from Japan*, 1997, **1**, 227–237.

41 R. M. Mihályi, Z. Schay and Á. Szegedi, *Catal Today*, 2009, **143**, 253–260.

42 S. S. Arzumanov, I. B. Moroz, D. Freude, J. Haase and A. G. Stepanov, *J Phys Chem C*, 2014, **118**, 14427–14432.

43 A. A. Gabrienko, S. S. Arzumanov, I. B. Moroz, I. P. Prosvirin, A. v Toktarev, W. Wang and A. G. Stepanov, *J Phys Chem C*, 2014, **118**, 8034–8043.

44 Z. Maeno, S. Yasumura, C. Liu, T. Toyao, K. Kon, A. Nakayama, J. Hasegawa and K. Shimizu, *Phys Chem Chem Phys*, 2019, **21**, 13415–13427.

45 Z. Maeno, S. Yasumura, X. Wu, M. Huang, C. Liu, T. Toyao and K. Shimizu, *J Am Chem Soc*, 2020, **142**, 4820–4832.

46 S. Yasumura, M. Huang, X. Wu, C. Liu, T. Toyao, Z. Maeno and K. Shimizu, *Catal Today*, 2020, **352**, 118–126.

47 M. Huang, S. Yasumura, L. Li, T. Toyao, Z. Maeno and K. Shimizu, *Catal Sci Technol*, 2022, **12**, 986–995.

48 Z. Maeno, X. Wu, S. Yasumura, T. Toyao, Y. Kanda and K. Shimizu, *Catalysts*, 2020, **10**. 807.

49 M. Huang, Z. Maeno, T. Toyao and K. Shimizu, *Catal Today*, DOI:https://doi.org/10.1016/j.cattod.2022.06.039.

50 M. H. Groothaert, P. J. Smeets, B. F. Sels, P. A. Jacobs and R. A. Schoonheydt, *J Am Chem Soc*, 2005, **127**, 1394–1395.

51 J. S. Woertink, P. J. Smeets, M. H. Groothaert, M. A. Vance, B. F. Sels, R. A. Schoonheydt and E. I. Solomon, *Proc Natl Acad Sci*, 2009, **106**, 18908–18913.

52 P. Vanelderen, B. E. R. Snyder, M.-L. Tsai, R. G. Hadt, J. Vancauwenbergh, O. Coussens, R. A. Schoonheydt, B. F. Sels and E. I. Solomon, *J Am Chem Soc*, 2015, **137**, 6383–6392.

53 S. Grundner, M. A. C. Markovits, G. Li, M. Tromp, E. A. Pidko, E. J. M. Hensen, A. Jentys, M. Sanchez-Sanchez and J. A. Lercher, *Nat Commun*, 2015, **6**, 7546.

54 C. Hammond, M. M. Forde, M. H. Ab Rahim, A. Thetford, Q. He, R. L. Jenkins, N. Dimitratos, J. A. Lopez-Sanchez, N. F. Dummer, D. M. Murphy, A. F. Carley, S. H. Taylor, D. J. Willock, E. E. Stangland, J. Kang, H. Hagen, C. J. Kiely and G. J. Hutchings, *Angew Chem Int Ed*, 2012, **51**, 5129–5133.

55 Y. Tang, Y. Li and F. (Feng) Tao, *Chem Soc Rev*, 2022, **51**, 376–423.

56 B. Wu, T. Lin, Z. Lu, X. Yu, M. Huang, R. Yang, C. Wang, C. Tian, J. Li, Y. Sun and L. Zhong, *Chem*, 2022, **8**, 1658–1672.

57 J. Shan, W. Huang, L. Nguyen, Y. Yu, S. Zhang, Y. Li, A. I. Frenkel and F. (Feng) Tao, *Langmuir*, 2014, **30**, 8558–8569.

58 N. v Beznis, B. M. Weckhuysen and J. H. Bitter, *Catal Lett*, 2010, **136**, 52–56.

59 H. K. Beyer, R. M. Mihályi, Ch. Minchev, Y. Neinska and V. Kanazirev, *Microporous Mater*, 1996, **7**, 333–341.

60 H. Solt, F. Lónyi, R. M. Mihályi, J. Valyon, L. B. Gutierrez and E. E. Miro, *J Phys Chem C*, 2008, **112**, 19423–19430.

61 G. Li, E. A. Pidko, R. A. van Santen, C. Li and E. J. M. Hensen, *J Phys Chem C*, 2013, **117**, 413–426.

62 S. Li, Y. Wang, T. Wu and W. F. Schneider, *ACS Catal*, 2018, **8**, 10119–10130.

63 C. Liu, G. Li, E. J. M. Hensen and E. A. Pidko, *ACS Catal*, 2015, **5**, 7024–7033.

64 Y. Tsuji and K. Yoshizawa, *J Phys Chem C*, 2018, **122**, 15359–15381.

65 J. Y. Saillard and R. Hoffmann, *J Am Chem Soc*, 1984, **106**, 2006–2026.

66 T. Kamachi, T. Tatsumi, T. Toyao, Y. Hinuma, Z. Maeno, S. Takakusagi, S. Furukawa, I. Takigawa and K. Shimizu, *J Phys Chem C*, 2019, **123**, 20988–20997.

67 A. A. Gabrienko, S. S. Arzumanov, A. v Toktarev, D. Freude, J. Haase and A. G. Stepanov, *J Phys Chem C*, 2011, **115**, 13877–13886.

68 H. Himei, M. Yamadaya, M. Kubo, R. Vetrivel, E. Broclawik and A. Miyamoto, *J Phys Chem*, 1995, **99**, 12461–12465.

69 E. Kikuchi, M. Ogura, I. Terasaki and Y. Goto, *J Catal*, 1996, **161**, 465–470.

70 G. D. Meitzner, E. Iglesia, J. E. Baumgartner and E. S. Huang, *J Catal*, 1993, **140**, 209–225.

71 E. J. M. Hensen, M. García-Sánchez, N. Rane, P. C. M. M. Magusin, P.-H. Liu, K.-J. Chao and R. A. van Santen, *Catal Lett*, 2005, **101**, 79–85.

72 A. P. Wilkinson, *Inorg Chem*, 1997, **36**, 1602–1607.

73 A. “Bean” Getsoian, U. Das, J. Camacho-Bunquin, G. Zhang, J. R. Gallagher, B. Hu, S. Cheah, J. A. Schaidle, D. A. Ruddy, J. E. Hensley, T. R. Krause, L. A. Curtiss, J. T. Miller and A. S. Hock, *Catal Sci Technol*, 2016, **6**, 6339–6353.

74 K. Nishi, K. Shimizu, M. Takamatsu, H. Yoshida, A. Satsuma, T. Tanaka, S. Yoshida

and T. Hattori, *J Phys Chem B*, 1998, **102**, 10190–10195.

75 C. Copéret, D. P. Estes, K. Larmier and K. Searles, *Chem Rev*, 2016, **116**, 8463–8505.

76 P. Serna and B. C. Gates, *Acc Chem Res*, 2014, **47**, 2612–2620.

77 J. Kondo, Y. Sakata, K. Domen, K. Maruya and T. Onishi, *J Chem Soc, Faraday Trans*, 1990, **86**, 397–401.

78 R. Wischert, P. Laurent, C. Copéret, F. Delbecq and P. Sautet, *J Am Chem Soc*, 2012, **134**, 14430–14449.

79 Z. Wu, Y. Cheng, F. Tao, L. Daemen, G. S. Foo, L. Nguyen, X. Zhang, A. Beste and A. J. Ramirez-Cuesta, *J Am Chem Soc*, 2017, **139**, 9721–9727.

80 H. Tsuneoka, K. Teramura, T. Shishido and T. Tanaka, *J Phys Chem C*, 2010, **114**, 8892–8898.

81 L. Wang, T. Yan, R. Song, W. Sun, Y. Dong, J. Guo, Z. Zhang, X. Wang and G. A. Ozin, *Angew Chem Int Ed*, 2019, **58**, 9501–9505.

82 M. K. Oudenhuijzen, J. A. van Bokhoven, J. T. Miller, D. E. Ramaker and D. C. Koningsberger, *J Am Chem Soc*, 2005, **127**, 1530–1540.

83 R. Juárez, S. F. Parker, P. Concepción, A. Corma and H. García, *Chem Sci*, 2010, **1**, 731–738.

84 A. Noujima, T. Mitsudome, T. Mizugaki, K. Jitsukawa and K. Kaneda, *Angewandte Chemie International Edition*, 2011, **50**, 2986–2989.

85 G. Tosin, M. Delgado, A. Baudouin, C. C. Santini, F. Bayard and J.-M. Basset, *Organometallics*, 2010, **29**, 1312–1322.

86 H. C. Foley, S. J. DeCanio, K. D. Tau, K. J. Chao, J. H. Onuferko, C. Dybowski and B. C. Gates, *J Am Chem Soc*, 1983, **105**, 3074–3082.

87 A. Bendjeriou-Sedjerari, J. M. Azzi, E. Abou-Hamad, D. H. Anjum, F. A. Pasha, K.-W. Huang, L. Emsley and J.-M. Basset, *J Am Chem Soc*, 2013, **135**, 17943–17951.

88 F. Rataboul, A. Baudouin, C. Thieuleux, L. Veyre, C. Copéret, J. Thivolle-Cazat, J.-M. Basset, A. Lesage and L. Emsley, *J Am Chem Soc*, 2004, **126**, 12541–12550.

89 D. P. Estes, G. Siddiqi, F. Allouche, K. v Kovtunov, O. v Safonova, A. L. Trigub, I. v Koptyug and C. Copéret, *J Am Chem Soc*, 2016, **138**, 14987–14997.

90 N. Kosinov, C. Liu, E. J. M. Hensen and E. A. Pidko, *Chem Mater*, 2018, **30**, 3177–3198.

91 H. Wang, L. Wang and F.-S. Xiao, *ACS Cent Sci*, 2020, **6**, 1685–1697.

92 V. B. Kazansky, A. I. Serykh, B. G. Anderson and R. A. van Santen, *Catal Lett*, 2003, **88**, 211–217.

93 A. Oda, H. Torigoe, A. Itadani, T. Ohkubo, T. Yumura, H. Kobayashi and Y. Kuroda,

Angew Chem Int Ed, 2012, **51**, 7719–7723.

94 S. Song, K. Yang, P. Zhang, Z. Wu, J. Li, H. Su, S. Dai, C. Xu, Z. Li, J. Liu and W. Song, *ACS Catal*, 2022, **12**, 5997–6006.

95 T. Baba, N. Komatsu, H. Sawada, Y. Yamaguchi, T. Takahashi, H. Sugisawa and Y. Ono, *Langmuir*, 1999, **15**, 7894–7896.

96 K. Khivantsev, A. Vityuk, H. A. Aleksandrov, G. N. Vayssilov, O. S. Alexeev and M. D. Amiridis, *J Phys Chem C*, 2015, **119**, 17166–17181.

97 E. Mansoor, M. Head-Gordon and A. T. Bell, *ACS Catal*, 2018, **8**, 6146–6162.

98 J. J. H. B. Sattler, J. Ruiz-Martinez, E. Santillan-Jimenez and B. M. Weckhuysen, *Chem Rev*, 2014, **114**, 10613–10653.

99 B. S. Kwak and W. M. H. Sachtler, *J Catal*, 1994, **145**, 456–463.

100 J. A. Biscardi and E. Iglesia, *Catal Today*, 1996, **31**, 207–231.

101 Y. Yuan, C. Brady, L. Annamalai, R. F. Lobo and B. Xu, *J Catal*, 2021, **393**, 60–69.

102 H. Saito and Y. Sekine, *RSC Adv*, 2020, **10**, 21427–21453.

103 S. De, S. Ould-Chikh, A. Aguilar, J.-L. Hazemann, A. Zitolo, A. Ramirez, S. Telalovic and J. Gascon, *ACS Catal*, 2021, **11**, 3988–3995.

104 Z. Yang, H. Li, H. Zhou, L. Wang, L. Wang, Q. Zhu, J. Xiao, X. Meng, J. Chen and F.-S. Xiao, *J Am Chem Soc*, 2020, **142**, 16429–16436.

105 H. Seki, H. Saito, K. Toko, Y. Hosono, T. Higo, J. Gil Seo, S. Maeda, K. Hashimoto, S. Ogo and Y. Sekine, *Appl Catal A Gen*, 2019, **581**, 23–30.

106 L.-C. Wang, Y. Zhang, J. Xu, W. Diao, S. Karakalos, B. Liu, X. Song, W. Wu, T. He and D. Ding, *Appl Catal B*, 2019, **256**, 117816.

107 T. Lei, Y. Cheng, C. Miao, W. Hua, Y. Yue and Z. Gao, *Fuel Process Technol*, 2018, **177**, 246–254.

108 T. V. M. Rao, E. M. Zahidi and A. Sayari, *J Mol Catal A Chem*, 2009, **301**, 159–165.

109 H. Guo, C. Miao, W. Hua, Y. Yue and Z. Gao, *Microporous Mesoporous Mater*, 2021, **312**, 110791.

110 Y. He, Y. Song and S. Laursen, *ACS Catal*, 2019, **9**, 10464–10468.

111 Z. Wu, E. C. Wegener, H.-T. Tseng, J. R. Gallagher, J. W. Harris, R. E. Diaz, Y. Ren, F. H. Ribeiro and J. T. Miller, *Catal Sci Technol*, 2016, **6**, 6965–6976.

112 Y. Xu, W. Hu, Y. Li, H. Su, W. Liang, B. Liu, J. Gong, Z. Liu and X. Liu, *ACS Catal*, 2023, 1830–1847.

113 J. Pan, J. Lee, M. Li, B. A. Trump and R. F. Lobo, *J Catal*, 2022, **413**, 812–820.

114 Y. G. Kolyagin, I. I. Ivanova, V. v Ordomsky, A. Gedeon and Y. A. Pirogov, *J Phys Chem C*, 2008, **112**, 20065–20069.

115 S. S. Arzumanov, A. A. Gabrienko, A. v Toktarev, Z. N. Lashchinskaya, D. Freude, J.

Haase and A. G. Stepanov, *J Phys Chem C*, 2019, **123**, 30473–30485.

116 A. L. Yakovlev, A. A. Shubin, G. M. Zhidomirov and R. A. van Santen, *Catal Lett*, 2000, **70**, 175–181.

117 J. R. di Iorio and R. Gounder, *Chem Mater*, 2016, **28**, 2236–2247.

118 V. Pashkova, P. Klein, J. Dedecek, V. Tokarová and B. Wichterlová, *Microporous Mesoporous Mater*, 2015, **202**, 138–146.

119 V. Gábová, J. Dědeček and J. Čejka, *Chem Commun*, 2003, 1196–1197.

120 J. Dědeček, Z. Sobalík and B. Wichterlová, *Catal Rev*, 2012, **54**, 135–223.